Effect of Concentration of Cerium in tin antimonide alloy

By

GOKILA.K

(14PPH005)

A dissertation submitted to

Avinashilingam Institute for Home Science and Higher Education for Women University

Coimbatore - 641 043.

In partial fulfillment of the requirements for degree of

Master of Science in Physics

April, 2016

Effect of Concentration of Cerium in tin antimonide alloy

By

GOKILA.K

(14PPH005)

A dissertation submitted to

Avinashilingam Institute for Home Science and Higher Education for Women

Coimbatore - 641 043.

In partial fulfillment of the requirements for degree of

Master of Science in Physics

April, 2016

29/4/16
Signature of Head of the Department

29/04/16
Signature of the Supervisor

ACKNOWLEDGEMENT

ACKNOWLEDGEMENT

I owe my sincere thanks to **Lord Almighty** and **My Lovable Parents** without whom I would have been nothing and showering their generous blessings upon me in all endeavors.

I wish to express my profound sense of gratitude **Shri**, **Dr.P.R.Krishnakumar**, Chancellor, Avinashilingam Institute for Home Science and Higher Education for Women, Coimbatore, for providing the facilities to conduct this study.

I extend my thanks to **Hon.Col.Dr. (Tmt.) Premavathy Vijayan,** M.Sc., M.Ed., Dip. Spl.Edn., M.Phil., Ph.D., Vice Chancellor (i/c), Avinashilingam Institute for Home Science and Higher Education for Women, Coimbatore, for providing flamboyant help towards the completion of the study.

I record my deep sense of gratitude and indebtedness to, **Dr. (Tmt.) A.Venmathi,** M.Sc, Dip.Ed, M.Phil, Ph.D. Registrar (i/c), Avinashilingam Institute for Home Science and Higher Education for Women, Coimbatore, for providing adequate help for the study.

I place on record my heartfelt thanks to **Hon.Col.Dr. (Tmt.) Saroja Prabakaran,** M.A.,Dip.Ed.,Ph.D.,Former Vice Chancellor, The Director, Hall of Residence, Avinashilingam Educational Trust Institutions Hostel, Coimbatore, for extending all possible help towards the completion of the study.

I gratefully record my sincere thanks to **Dr. (Tmt.) A. Parvathi**, M.Sc.,Dip. Ed., M.Phil., Ph.D., Dean, Faculty of Science, Avinashilingam Institute for Home Science and Higher Education for Women, Coimbatore, for timely help rendered throughout the course.

I whole heartily thank **Dr. (Tmt.) J. Shanthi,** M.Sc., M.Phil., Ph.D., Associate Professor and Head of the Department of Physics, Avinashilingam Institute for Home Science and Higher Education for Women, Coimbatore, for her encouragement and generous help which was of great value.

I express my heartiest thanks to my guide **Dr. (Tmt.) B.Nalini,** M.Sc., Ph.D., M.S (Edu.Mgt.), STA Fellow, AIST Fellow (Japan), Assistant Professor, Department of Physics, Avinashilingam Institute for Home Science and Higher Education for Women, Coimbatore, for her inspiring guidance, meticulous care, patience, help, encouragement, motivation, and skillful and expert suggestions in completion of this work.

I sincerely thank all **the staff members** of the Department of Physics, Avinashilingam Institute for Home Science and Higher Education for Women, Coimbatore, for their help and support.

I would like to express my special thanks to **my parents**, **brother**, **sister**, **my friends** and all **my well wishers** for their constant encouragement, support and help in carrying out this work successfully.

GOKILA.K

CONTENT

CONTENT

LIST OF FIGURES

LIST OF TABLES

INTRODUCTION

CHAPTER I

INTRODUCTION

1. Introduction

A Phosphor is a substance that exhibits the phenomenon of luminescence this includes phosphorescent materials and fluorescent materials. Phosphorescent materials show a slow decay in brightness; this is used in radar screens and glow in the dark toys. Fluorescent material takes ten Nanoseconds for the emission decay and these materials are employed in cathode ray tube and plasma video display screens, sensors, and white LEDs. Phosphors are often transition metal or rare earth compounds of various types. Phosphorus the chemical element named for its light emitting behavior emits light due to chemiluminescence not phosphorescence [1]. A material can emit light either through incandescence, where all atoms radiate, or by luminescence where only a small fraction of atoms called emission centers or luminescence centers, emit light. In inorganic phosphors , the homogeneities in the crystal structure are created usually by addition of a trace amount of dopant and impurities called activators.

The scintillation process in inorganic materials is due to the electronic band structure found in the crystals. An incoming particle can excite an electron from the valence band to the conduction band . This leaves an associated hole behind, in the valence band. Impurities create electronic levels in the forbidden gap. In case of inorganic scintillators, the activator impurities are typically chosen so that the emitted light is in the visible range or near-UV where photomultipliers are effective. The holes associated with electrons in the conduction band are independent from the latter. Those holes and electrons are captured successively by impurity centers exciting certain metastable states not accessible to the excitons. The delayed de-excitation of those metastable impurity states, slowed down by reliance on the low-probability forbidden mechanism, again results in light emission. Many phosphors tend to lose its efficiency in several mechanisms. The degradation of electroluminescent devices depends on frequency of driving current, luminance level and temperature. Harder, high melting, water insoluble materials display lower tendency to lose luminescence under operation [2].

1.1 Materials

Phosphors are made from a suitable host material with an added activator. The host materials are typically oxides, nitrides and oxynitrides [3], sulfides, selenides, halides or silicates of zinc, cadmium, manganese, aluminium, silicon or various earth metals. Phosphors used for fluorescent lamps require a multi-step production process, with details that vary depending on the particular phosphor. Bulk material must be milled to obtain a desired particle size range, since large particles produce a poor quality lamp coating and small particle produce less light and degrade more quickly. During the firing of the phosphor, process conditions must be controlled to prevent oxidation of the phosphor activators or contamination from the process vessels. After milling the phosphor may be washed to remove minor excess of activator elements. Volatile elements must not be allowed to escape during processing. Lamp manufacturers have changed composition of phosphors to eliminate some toxic elements, such as beryllium, cadmium, or thallium, formerly used [4].

1.1.1 Application

- Lighting
- Phosphor thermometry
- Glow in the dark toys
- Radio luminescence
- Electroluminescence

Lighting: Phosphor layers provide most of the light produced by fluorescent lamps, and are also used to improve the balance of light produced by metal halide lamps. Various neon signs use phosphor layers to produce different colors of light. Electroluminescent displays. White LED lamps consist of a blue or ultra-violet emitter with a phosphor coating that emits at longer wavelengths, giving a full spectrum of visible light. Example: aircraft instrument panels, numeric and graphic display devices.

Phosphor thermometry: Phosphor thermometry is a temperature measurement approach that uses the temperature dependence of certain phosphors. Phosphor coating is applied to the surface and the decay time is the emission parameter that indicates temperature. Also, phosphor may be applied to the end of an optical fiber as an optical analog of a thermocouple.

Glow in the dark toys: Calcium sulfide with strontium sulfide with bismuth as activator, (Ca,Sr) S:Bi, yields blue light with glow times up to 12 hours, red and orange are modifications of the zinc sulfide formula. Red color can be obtained from strontium sulfide, Zinc sulfide with about 5 ppm of a copper activator is the most common phosphor for the glow-in-the-dark toys and items. It is also called **GS** phosphor, Mix of zinc sulfide and cadmium sulfide emit color depending on their ratio; increasing of the CdS content shifts the output color towards longer wavelengths; its persistence ranges between 1–10 hours.

Radioluminescence: Zinc sulfide phosphors are used with radioactive materials, where the phosphor was excited by the alpha- and beta-decaying isotopes, to create luminescent paint for dials of watches and instruments. Tritium is also used as a source of radiation in various products utilizing tritium illumination.

Electroluminescence: Electroluminescence exploited in light source and emit from a large area, which makes them suitable for backlights of LCD display.

1.2 Rare earth elements

The rare earth elements (REEs), which include the 15 lanthanide elements (Z = 57 through 71) and yttrium (Z = 39), most of them are originally isolated in the 18th and 19th centuries as oxides from rare minerals [5].

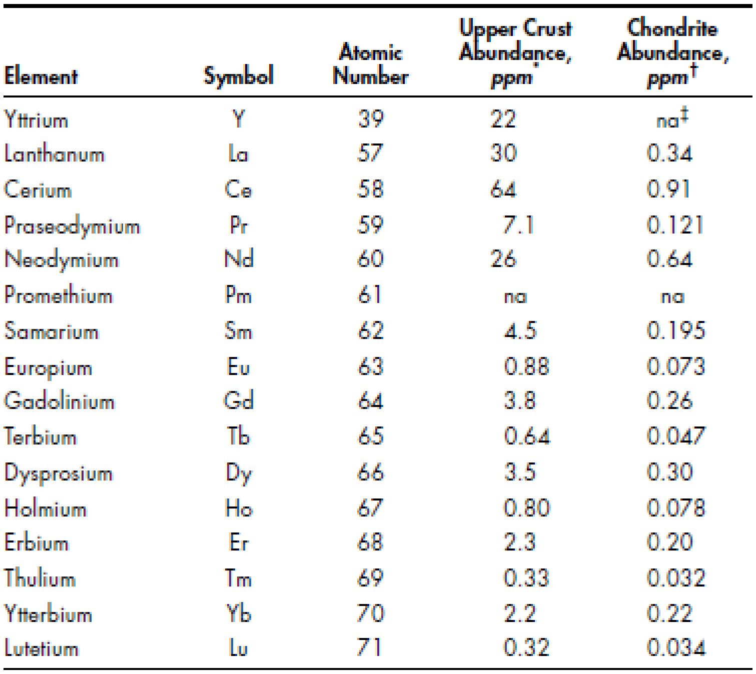

Element	Symbol	Atomic Number	Upper Crust Abundance, ppm*	Chondrite Abundance, ppm†
Yttrium	Y	39	22	na‡
Lanthanum	La	57	30	0.34
Cerium	Ce	58	64	0.91
Praseodymium	Pr	59	7.1	0.121
Neodymium	Nd	60	26	0.64
Promethium	Pm	61	na	na
Samarium	Sm	62	4.5	0.195
Europium	Eu	63	0.88	0.073
Gadolinium	Gd	64	3.8	0.26
Terbium	Tb	65	0.64	0.047
Dysprosium	Dy	66	3.5	0.30
Holmium	Ho	67	0.80	0.078
Erbium	Er	68	2.3	0.20
Thulium	Tm	69	0.33	0.032
Ytterbium	Yb	70	2.2	0.22
Lutetium	Lu	71	0.32	0.034

Table 1 REEs, atomic number, and abundance

All of the REEs were finally identified in the 20th century. Promethium, the rarest, was not identified until 1945, and pure lutetium metal was not refined until 1953 (Emsley 2001). Commercial markets for most of the REEs have arisen in only the past 50 years. Most REEs are not as uncommon in nature as the name implies. Cerium, the most abundant REE (Table 1), comprises more of the earth’s crust than copper or lead. Many REEs are more common than tin and molybdenum, and all but promethium are more common than silver or mercury (Taylor and McClennan 1985). Promethium, best known as an artificial element, occurs in very minute quantities in natural materials because it has no stable or long-lived isotopes. Lanthanide elements with low atomic numbers are generally more abundant in the earth’s crust than those with high atomic numbers. Those with even atomic numbers are two to seven times more abundant than adjacent lanthanides with odd atomic numbers (Table 1). The lanthanide elements traditionally have been divided into two groups: the light rare earth elements (LREEs)—lanthanum through europium (Z = 57 through 63); and the heavy rare earth elements (HREEs)—gadolinium through lutetium (Z = 64 through71). Although yttrium is the lightest REE, it is usually grouped with the HREEs to which it is chemically and physically similar. The REEs are lithophile elements (elements enriched in the earth’s crust) that invariably occur together naturally because all are trivalent (except for Ce^{+4} and Eu^{+2} in some environments) and have similar ionic radii. An increase in atomic number in the lanthanide group is not accompanied by change in valence, and the lanthanide elements all inhabit the same cell in most versions of the periodic table. The similar radii and oxidation states of the REEs allow for liberal substitution of the REEs for each other into various crystal lattices. This substitution accounts for their wide dispersion in the earth's crust and the characteristic multiple occurrences of REEs within a single mineral. The chemical and physical differences that exist within the REEs group are caused by small differences in ionic radius and generally result in segregation of REEs into deposits enriched in light lanthanides or heavy lanthanides plus yttrium. The relative abundance of individual lanthanide elements has been found useful in the understanding of magmatic processes and natural aqueous systems. Comparisons are generally made using a logarithmic plot of lanthanide abundances normalized to abundances in chondritic (stony) meteorites. The use of this method eliminates the abundance variation between lanthanides of odd and even atomic number, and allows determination of the extent of fractionation between the lanthanides, because such fractionation is not considered to have taken place during chondrite formation. The method also is useful because chondrites are thought to be compositionally similar to the original earth's mantle. Europium (Eu) anomalies (positive or negative departures of europium from chondrite normalized plots) have been found to be particularly effective for petrogenetic modeling. In addition, REE isotopes, particularly of neodymium and samarium, have found use in petro genetic modeling and geochronology [5].

1.2.1 Minerals That Contain REE:

REEs comprise significant amounts of many minerals; almost all production has come from less than 10 minerals. Extraction from a potentially economic REE resource is strongly dependent on its REE mineralogy. In the past, producing deposits were limited to those containing REE bearing minerals that are relatively easy to concentrate because of coarse grain size or other attributes. Minerals that are easily broken down, such as the carbonate bastnasite, are more desirable than those that are difficult to dissociate, such as the silicate allanite. Placer monazite, once an important source of REEs, has been largely abandoned because of its high thorium content. Recently, REEs absorbed on clay minerals in laterite have become important sources of REEs [5].

1.2.2 Cerium

Cerium is the most abundant of the rare earth metals. Rare earth metals are the elements in Row 6 of the periodic table. It is a gray metal that easily reacts with other elements, used in making a number of different alloys, in the production of many kinds of speciality glass, and in the chemical industry. Cerium was the first rare earth element to be discovered. It was isolated in 1839 by Swedish chemist Carl Gustav Mosander (1797-1858). Mosander was studying a new rock that had been discovered outside the town of Bastnas, Sweden. Mosander named the new element cerium, in honor of the asteroid Ceres that had been discovered in 1801.

It has the Symbol: Ce

Atomic number : 58

Atomic mass : 140.12

Family : Lanthanide (rare earth elements)

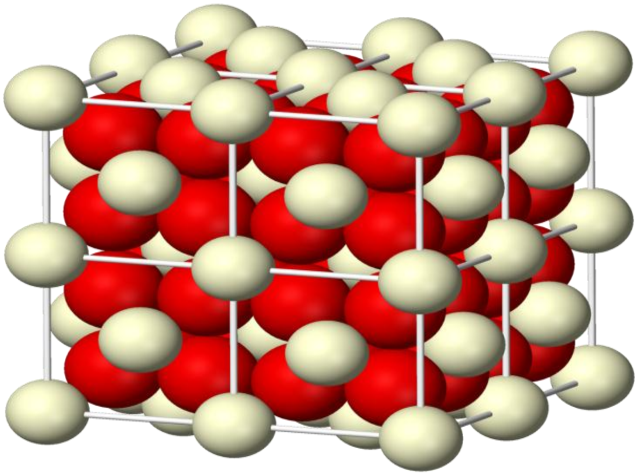

Figure 1.1 Cerium

1.2.3 Physical properties

Cerium is an iron-gray metal with a melting point of 795°C (1,460°F) and a boiling point of 3,257°C (5,895°F). It is ductile and malleable. Ductile means capable of being made into thin wires. Malleable means capable of being hammered into thin sheets. Cerium's density is 6.78 grams per cubic centimeter. It exists in four different allotropic forms. Allotropes are forms of an element with different physical and chemical properties.

Chemical properties

Cerium is the second most active lanthanide after europium. Cerium reacts so readily with oxygen that it can be set on fire simply by scratching the surface with a knife. It also reacts with cold water (slowly), hot water (rapidly), acids, bases, hydrogen gas, and other metals. Because it is so active, it must be handled with caution.

Occurrence in nature

The most important ores of cerium are cerite, monazite, and bastnasite. It is thought to occur in the Earth's crust with a concentration of 40 to 66 parts per million. This makes cerium about as abundant as **copper** or **zinc.**

Isotopes

Four naturally occurring isotopes of cerium have been discovered: cerium-136, cerium-138, cerium-140, and cerium-142. The last of these isotopes is radioactive. Isotopes are two or more forms of an element. Isotopes differ from each other according to their mass number. The number written to the right of the element's name is the mass number. The mass number represents the number of protons plus neutrons in the nucleus of an atom of the element. The number of protons determines the element, but the number of neutrons in the atom of any one element can vary. Each variation is an isotope. A radioactive isotope is one that breaks apart and gives off some form of radiation.

1.2.4 Uses and compounds

Cerium metal and its compounds have a great variety of uses, many in the field of glass and ceramics. Cerium and its compounds are added to these materials to add color (yellow), remove unwanted color, make glass sensitive to certain forms of radiation, add special optical (light) qualities to glass, and strengthen certain kinds of dental materials. Important new applications are being found for cerium lasers. A laser is a device that produces bright light of a single frequency or color. Cerium lasers contain a crystal made of **lithium, strontium, aluminum,** and **fluorine,** to which a small amount of cerium is added. A cerium laser produces light in the ultraviolet region. Cerium lasers are used to search for ozone and sulfur dioxide, two air pollutants, in the atmosphere. Cerium compounds are also used in making phosphors. A phosphor is a material that shines when struck by electrons. The color of the phosphor depends on the elements of which it is made. Phosphors that contain cerium compounds produce a red or orange light when struck by electrons. Cerium is also used in catalytic systems. A catalyst is a substance used to speed up or slow down a chemical reaction. The catalyst does not undergo any change by itself during the reaction. Compounds of cerium are used in the refining of petroleum. They help break down compounds found in petroleum into simpler forms that work better as fuels. Another application of cerium (in the form of cerium oxide) is in internal combustion engines, like the one found in cars. Adding cerium oxide (CeO_2) to the engine's fuel helps the fuel burn more cleanly, producing fewer pollutants.

Cerium lasers are used to search for ozone and sulfur dioxide, two air pollutants, in the atmosphere. A number of alloys contain cerium. An alloy is made by melting and mixing two or more metals. The mixture has properties different from those of the individual metals. Perhaps the best known alloy of cerium is misch metal. Misch metal contains a number of different rare earth elements and has the unusual property of giving off a spark when struck. It is used, for example, in the flint of a cigarette lighter. Cerium oxide is also used as an abrasive. An abrasive is a powdery material used to grind or polish other materials. Cerium oxide has replaced an older abrasive known as rouge for polishing specialized glass, such as telescope mirrors [6].

1.2.5 Fuel cell electrolyte

In the doped form (it comes from cerium and oxygen), ceria is of interest as a material for solid oxide fuel cells or SOFCs because of its relatively high oxygen ion conductivity (i.e. oxygen atoms readily move through it) at intermediate temperatures (500–650 °C). Undoped and doped ceria also exhibit high electronic conductivity at low partial pressures of oxygen due to reduction of the cerium ion leading to the formation of small polarons. However, doped ceria has an extended electrolytic region (area of predominant ionic conductivity), over that of ceria, that allows its use as an electrolyte in SOFCs below 600-650 °C. Exposure to hydrogen at high temperature (800 °C) has been shown to cause significant damage to the grain boundaries leading to cracking. Exposure to other reducing agents such as carbon monoxide is less damaging [7]. Substituting a fraction of the ceria with gadolinium (as in Gadolinium doped ceria) or samarium will introduce oxygen vacancies in the crystal without adding electronic charge carriers. This increases the ionic conductivity and results in a better electrolyte.

Under reducing conditions, such as those experienced on the anode side of the fuel cell, a large amount of oxygen vacancies within the ceria electrolyte can be formed. Some of the cerium (IV) oxide is also reduced to cerium (III) oxide under these conditions, which consequently increases the electronic conductivity of the material [7]. The lattice constant of ceria increases under reducing conditions as well as with decreasing nanocrystal size in nanocrystalline ceria, as a result of reduction of the cerium cation from 4+ to 3+ state in order to charge compensate for oxygen vacancy formation[8].

1.3 Antimony

Antimony is a metalloid, so it has some metallic properties but not enough to be classified as a true metal. Physically, it behaves like sulfur while chemically it is more metallic [9]. Its electrical and thermal conductivity are lower than most metals' conductivities. Antimony is a brittle, fusible, crystalline solid. It is easily powdered. And also has the unusual property that (like water) it expands as it freezes. Four other elements expand when they freeze; silicon, bismuth, gallium and germanium. In addition to the usual form of antimony, there are two allotropes: yellow crystalline and amorphous black.

Name : Antimony

Symbol : Sb

Type : Metalloid Nitrogen group

Atomic weight : 121.75

Atomic volume: 18.22cm^3/mol

Colour : Silvery white

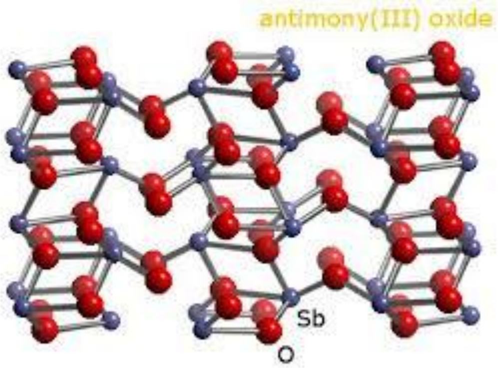

Figure 1.2.Antimony

1.3.1Application

The major use of antimony is in lead alloys - mainly for use in batteries - adding hardness and smoothness of finish. The higher the proportion of antimony in the alloy, the harder and more brittle it will be. Alloys made with antimony expand on cooling, retaining the finer details of molds. Antimony alloys are therefore used in making type faces for clear, sharp printing. Babbit metals, used for machinery bearings, are alloys of lead, tin, copper and antimony. These metals are hard but slippery and so ideal for use as bearings [10] Antimony is used in the semiconductor industry as an n-type dopant for silicon. Antimony trioxide is used as a flame retardant in adhesives, plastics, rubber and textiles.

1.3.2 Health effects of Antimony

Human exposure to antimony can take place by breathing air, drinking water and eating foods that contain it, but also by skin contact with soil, water and other substances that contain it.

Breathing in antimony that is bond to hydrogen in the gaseous phase, is what mainly causes the health effects. Exposure to relativity high concentration of antimony (9 mg/$m^3$of air) for a long period of time can cause irritation of the eyes, skin and lungs. Antimony is used as a medicine for parasital infections.

1.4 Tin

Tin is a soft, pliable, silvery-white metal. Tin is not easily oxidized and resists corrosion because it is protected by an oxide film. Tin resists corrosion from distilled sea and soft tap water, and can be attacked by strong acids, alkalis and acid salts.

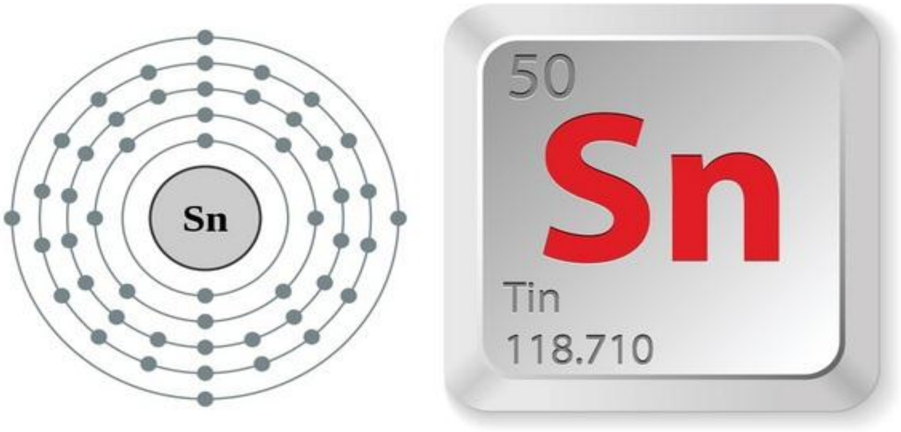

Figure 1.3.Tin structure

Symbol : Sn

Atomic number: 50

Atomic mass : 118.69g.mol^{-1}

Melting point : 232^0C

Boiling point : 2270^0C

1.4.1 Physical properties

The most common allotrope of tin is a silver white metallic looking solid known as the β form. Allotropes are forms of an element with different physical and chemical properties. One of tin's properties is its tendency to give off a strange screeching sound when it is bent. This sound is known as "tin cry", β-tin is both malleable and ductile.

1.4.2 Chemical properties

Tin is relatively unaffected by both water and oxygen at room temperature. It does not rust, corrode, or react in any other way. Tin is attacked only slowly by dilute such as hydrochloric acid and sulfuric acid. Dilute acids are mixtures that contain small amount of acids dissolved in large amounts of water. This property also makes tin a good protective covering. It does not react with acids as rapidly as do many other kinds of metals such as iron, and can be used, therefore as a covering for those metals. It forms compounds with sulfur, selenium, and tellurium.

1.4.3 Effects of Tin on the Environment

Organic tins can spread through the water systems when adsorbed on sludge particles. They are known to cause a great deal of harm to aquatic ecosystems, as they are very toxic to fungi, algae and phytoplankton. Phytoplankton is a very important link in the aquatic ecosystem, as it provides other water organisms with oxygen. It is also an important part of the aquatic food chain. There are many different types of organic tin that can vary greatly in toxicity. Tributyltins are the most toxic tin components to fish and fungi, whereas trifenyltin is much more toxic to phytoplankton. Organic tins are known to disturb growth, reproduction, enzymatic systems and feeding patterns of aquatic organisms. The exposure mainly takes place in the top layer of the water, as that is where organic tin compounds accumulate.

1.4.4 Health effects of Tin

Tin is mainly applied in various organic substances. The organic tin bonds are the most dangerous forms of tin for humans. Despite the dangers they are applied in a great number of industries, such as the paint industry and the plastic industry, and in agriculture through pesticides. The number of applications of organic tin substances is still increasing, despite the fact that we know the consequences of tin poisoning. The effects of organic tin substances can vary. They depend upon the kind of substance that is present and the organism that is exposed to it. Triethyltin is the most dangerous organic tin substance for humans. It has relatively short hydrogen bonds. When hydrogen bonds grow longer a tin substance will be less dangerous to human health. Humans can absorb tin bonds through food and breathing and through the skin. The uptake of tin bonds can cause acute effects as well as long-term effects. **Effects:** Eye and Skin irritations, Headaches, Stomachaches, Sickness and dizziness, Severe sweating, Breathlessness, Urination problems.

1.4.5 Applications

Tin is used in for can coating: tin-plated steel containers are widely used for food preservation. Tin alloys are employed in many ways: as solder for joining pipes or electric circuits, pewter, bell metal, babbit metal and dental amalgams. The niobium-tin alloy is used for superconductiong magnets, tin oxide is used for ceramics and in gas sensors (as it absorbs a gas its electrical conmductivity increases and this can be monitored). Tin foil was once a common wrapping material for foods and drugs, now replaced by the use of aluminium foil.

1.5 Objective of the present work

The Alloys is nanoparticle range will be very useful in tailored emission or phosphorescence behavior. And rare earths would be a good additive to improve the emission profile of nano materials. Hence the objective is to study the luminescence profile of tin-antimony doped with cerium (rare earth).

1.6 REFERENCE

1. Emsley,John(2000),The Shocking History of Phosphorus, London: Macmillan, ISBN 0-330-39005-8.

2. Peter W.Hawkes (1 October 1990). Advances in electronics and electron physics, Academic Press.pp.350-ISBN 978-0-12-014679-6.Retrived 9 January 2012.

3.Xie,Rong-Jun;Hirosaki,Naoto (2007).Silicon based oxynitride and nitride phosphors for white LEDs-A review.Sci.Technol.Adv.Mater.8(7-8);588.

4. Raymond Kane, Heinz Sell Revolution in lamps: a chronicle of 50 years of progress(2nd ed),The Fairmont Press,Inc.2001ISBN 0-88173-378-4.Chapter 5 extensively discusses history ,application and manufacturing of phosphors for lamps.

5. Stephen B.Castor ,James B.Hedrick, Rare earth elements,(769-792)

6. "Cerium (revised)." Chemical Elements: From Carbon to Krypton. 2006. Encyclopedia.com. 4 Mar. 2016 <http://www.encyclopedia.com>.

7.Zholobak,N.M; Ivanov,V.K; Shcherbakov, A.B;Shaporev A.S; Polezhaeva, O.S; Baranchikov, A.Ye.; Spivak, N.Ya.; Tretyakov, Yu.D. (2011). "UV-shielding property, photocatalytic activity and photocytotoxicity of ceria colloid solutions". Journal of Photochemistry and Photobiology B: Biology **102** (1): 32–38. doi:10.1016/j.jphotobiol.2010.09.002.

8. "Suncream may be linked to Alzheimer's disease, say experts". Daily Mail (London). 24 August 2009. Retrieved 2009-08-25.

9. Robert E. Krebs, The history and use of our earth's chemical elements: a reference guide., (2006) p219. Greenwood Publishing Group

10. George Stuart Brady, Henry R. Clauser, John A. Vaccari Materials Handbook., (2002) p74. McGraw Hill Professional

REVIEW OF LITERATURE

CHAPTER II

REVIEW OF LITERATURE

2.1 Literature Review

1) J.Schoonman(2003) Nanostructured materials are distinguished from conventional polycrystalline materials by the size of the structural units that compose them, and they often exhibit properties that are drastically different from the polycrystalline materials. In many instances, this can be related to large fractions of grain boundaries and hence large numbers of surface atoms. Defect thermodynamics in the bulk may then be governed by surfaces. As tailoring of fundamental properties becomes possible in the quantum confinement regime, existing materials may find new applications. In this review, recent studies of the properties of nanostructured electroceramics is presented. The applications relate to electrochemical devices for energy conversion and storage. A breakthrough in metal hydride technology is achieved by preparing nanostructured hydride forming materials. In addition, several forms of carbon are being studied for hydrogen storage. Alkali-doped carbon nanotubes and nanosized SiC powders are promising as well. Consolidation of nanosized powders by dynamic compaction techniques leads to nanostructured microstructures. Recent examples using Magnetic Pulse Compaction (MPC) are presented.

2) Lavinia Balan *et al*.,(2005) Monodisperse SnSb alloy nanoparticles are prepared by reduction of $SnCl_2$ and $SbCl_5$ using *t*-BuONa activated NaH. The morphology and the structure of the nano-alloy are examined by transmission electron microscopy (TEM), selected-area electron diffraction (SAED), X-ray diffraction (XRD) and X-ray photoelectron spectroscopy (XPS). The result shows that very small rhombohedral nanoparticles with an average diameter of 4.7 ± 0.1nm were produced. This route provides a promising candidate for studying capacities of nanosized SnSb alloys in electrochemical energy storage devices.

3) J.K.O.Asante *et al*.,(2005) Surface segregation studies of Sn and Sb in Cu(1 0 0)–0.14 at.% Sn–0.12 at.%Sb ternary alloy, have been done by making use of Auger Electron Spectroscopy. The method of Linear Temperature Ramp (LTR) is employed, whereby the sample is heated and cooled linearly at a constant rate. The positive heating rate shows both a kinetic segregation profile, as well as a narrow equilibrium segregation region, at higher temperatures. The equilibrium segregation profile is extended by cooling the sample. Sn is the first to segregate to the surface due to its higher diffusion coefficient, mainly from smaller activation energy E_{Sn}, Sb, due to its higher segregation energy, eventually replaced Sn from the surface. The modified Darken model is used to simulate the profile yielding the following segregation parameters: $Do_{(Sn)} = 6.3\times10^{-6} m^2/s$, $Do_{(Sb)} = 2.8\times10^{-5}\ m^2/s$; E_{Sn} = 175.4 kJ/mol, E_{Sb} = 186.3 kJ/mol; $V_{Cu–Sn}$ =3.4 kJ/mol, $V_{Cu–Sb}$ = 15.9 kJ/mol and $V_{Sn–Sb}$ = -5.4 kJ/mol.

4) Hong Guo *et al*.,(2006) Microscaled Si/SnSb alloy composite is synthesized from micron Si and oxides of Sn and Sb by carbothermal reaction method. The synthesized Si/SnSb composite electrode exhibits a high specific capacity and a good cycling stability due to its relatively large particle size and multi-phase characteristics. The former reason leads to lower surface impurity and thus the lower initial capacity loss, while the latter results in a stepwise lithiation/delithiation process and a smooth volume change of electrode in cycles. Si/SnSb composite shows an initial inertia against the electrochemical reactions. A specific capacity of 1017 mAh g^{-1} with an initial capacity loss of 120 mAh g^{-1} is achieved for the synthesized Si/SnSb composite.

5) Ge Zhang *et al*.,(2006) Cu_2Sb, SnSb and Sn/SnSb mesoscopic alloy powders are prepared by chemical reduction, respectively. The crystal structures and particle morphology of Cu_2Sb, SnSb and Sn/SnSb are characterized by X-ray diffraction (XRD), scanning electron microscopy (SEM). The electrochemical performances of the Cu_2Sb, SnSb and Sn/SnSb electrodes are investigated by galvanostatic charge and discharge cycling and electrochemical impedance spectroscopy (EIS). The results shows the first charge and discharge capacities of SnSb and Sn/SnSb are higher than Cu_2Sb, the charge capacity fading rates of Cu_2Sb, Sn/SnSb and Sn/SnSb are 26.16%, 55.33% and 47.39%, respectively. Cu_2Sb had a better cycle performance, and Sn/SnSb multiphase alloy is prior to pure SnSb due to the existence of excessive Sn in Sn/SnSb system.

6) Jyh-Ming Wu (2008) Sb doped SnO_2 (SnO_2:Sb) nanowires (NWs) are synthesized by thermal evaporation at 900 °C. Thin-film X-ray diffraction showed that as synthesized Nano wires shows a single-phase rutile structure. Field emission scanning microscopy reveals that the nanowires had diameters of 80–120 nm and lengths of up to several hundred microns long. High-resolution transmission electron microscopy (HRTEM), electron energy-loss spectroscopy (EELS), and an energy-filtering system are employed to map two-dimensional element concentration. HRTEM images further confirmed that the crystallinity of the nanowires is accompanied by crystal defects with lattice distortion as Sb is incorporated into a SnO_2 nanowire. Cathodoluminescence

(CL) spectrophotometer analysis has revealed blue and green emission peaks in both SnO_2: Sb and pure SnO_2 nanowires. The electron field emission values of the SnO_2: Sb and SnO_2 nanowires in the turn on fields were estimated as ~4.9 and 6.5 V/μm, respectively; the current density was 1 $\mu A/cm^2$.

7) L.K.Dua *et at*.,(2008) Antimony doped tin oxide (ATO) films of 326–1714±3Å physical thickness is deposited on to silica glass substrate by the sol–gel spinning technique. The chosen atomic ratios of Sn: Sb is varied as 90:10, 70:30, 50:50 and 30:70. Nano structured surface feature is observed in the SEM micrographs of ATO films of 10 to 30 at. % Sb. The nano cluster size is dependent on antimony content. Cassiterite phase of SnO_2 is observed at low content of Sb. The films are absorbing in the UV region. Two direct band gaps and one indirect band gap for each system are evaluated from their absorption spectra. The two direct band gap values are in the range, 3.73–5.20 eV while the indirect band gap values are in the range, 2.54–3.46 eV. In the case of single layer system, Moss–Burstein shift in both direct and indirect band gaps is observed with increase in at.% of Sb content. Electrical resistivity of the films is in the range, 1.19×10^{-3} to 155.59×10^{-3} Ω cm. Minimum resistivity was obtained for 30 at.% Sb. Transmissivity of the films in the visible region is in the range, 80–97%. Total thermal emissivity (λ range, 5.0–20.0 μm) values are in the range 0.78–0.86.

8) Navida Nasir *et al*.,(2009) phase relations in the ternary systems Ce-M-Sb in composition regions $CeSb_2$-Sb-M are studied optical and electron microscopy, X-ray Diffraction and electron probe microanalysis on arc-melted alloys and specimens annealed in the temperature region from 850 to 200^0 C. There is no ternary compound in the form Ce-Si-Sb.

9) Fei Wang *et al*.,(2009) Nano-sized SnSb alloy anodes are prepared by reductive co-precipitation method combining with the aging treatment in water bath at 80 °C. The microstructure, morphology and electrochemical properties of synthesized SnSb alloy powders are evaluated by X-ray diffraction (XRD), field-emission scanning electron microscopy (FE-SEM) and galvanostatical cycling tests. The result indicates that the cycling performance of SnSb alloy anodes could be improved through reducing particle size. The capacity decline was still apparent in every cycle due to the poor reversible process of high voltage reaction. When the cut-off potential is limited between 0.02 and 0.9 V, the volume and structure changes are alleviated effectively and the excellent cycling performance is obtained within 20 cycles.

10) Lili Gao *et al*.,(2010) Recent years, the SnAgCu family of alloys has been found a widely application as a replacement for the conventional SnPb solders in electronic industry. In order to further enhance the properties of SnAgCu solder alloys, alloying elements such as rare earth, Bi, Sb, Fe, Co, Mn, Ti, In, Ni, Ge and nano-particles are selected by lots of researchers as alloys addition into these alloys. Rare earth (RE) elements have been called the ‘‘vitamin” of metals, which means that a small amount of RE elements can greatly enhance the properties of metals, such as microstructure refinement, alloying and purification of materials and metamorphosis of inclusions. In addition, a small amount of Zn addition has the ability to reduce undercooling efficiently and suppress the formation of massive primary Ag_3Sn plates, and Bi/Ga has the ability to enhance the wettability of SnAgCu alloys as well as Ni. Moreover, adding Co/Fe/Ge can effectively refine microstructure, modify interfacial Cu–Sn compounds and increase the shear strength of joints with Cu. This paper summarizes the effects of alloying elements on the wettability, mechanical properties, creep behavior and microstructures of SnAgCu lead-free solder alloys.

11) Sonia Rodriguez-Liviano *et al*.,(2011) Mesoporous tetragonal RE:YPO_4 nanophosphors (RE =Eu, Ce, Tb, and Ce + Tb) with a lenticular morphology, narrow size distribution, and high surface area have been prepared by an homogeneous precipitation procedure consisting of aging, at low temperature (80−120 °C) in a microwave oven, ethylene glycol solutions containing only yttrium acetylacetonate and phosphoric acid. This synthesis method involves important advantages such as its simplicity, rapidness (reaction time = 7 min), and high reaction yields. The mechanism of nanoparticle growth has been also addressed finding that the lenticular nanoparticles are formed through an ordered aggregation of smaller entities, which explains their porosity. In all cases, the doping levels were systematically varied in order to optimize the nanophosphors luminescence. All optimum nanophosphors presented a high luminescence quantum yield (QY). In particular, for the Eu and Tb doped systems, the obtained QY values (60% for Eu and 80% for Tb) are the highest so far reported for this kind of nanomaterial. The morphological, microstructural, and luminescent properties of this nanophosphors and their dispersibility in water make them suitable for biomedical applications.

12) Feng Dan Wu *et al*.,(2011) Antimony-doped tin oxide (ATO) nanotubes are synthesized by a modified template method in this work. The nanotubes, which are ~200 nm in diameter and

10–20 nm in wall thickness, are composed of a large number of 5–15 nm ATO nanocrystals. The doping level of Sb in the ATO could be varied by the experimental conditions. ATO nanotubes with Sn:Sb ratios of 9:1 or 5:1, in particular, are good reversible Li storage materials, shows high capacities and good cyclability at both common and high rates of charge and discharge.

13) Jun-ichi Tani *et al*.,(2012) have studied the formation energy and atomic structure of impurities in Mg_2Sn using first-principles plane-wave total energy calculations. Twenty elements, namely H, Li ,Na ,K ,Rb ,Sc ,Y ,La ,Cu ,Ag ,Au ,B, Al, Ga ,In ,N ,P ,As ,Sb ,and Bi, are selected as the impurity species. They considered structural relaxation of the atoms within the second nearest neighbors of the impurity atom in the 48-atom super cell. The results of the formation energy calculations suggested that Sc, Y, La, P, As, Sb, and Bi are good n-type dopants whereas Li and Na are good p-type dopants. The electrical properties of Li-,Na-,and Ga-doped Mg_2Sn and La-dopedMg_2(Si, Sn)composites reported previously can be explained by the low formation energies of Li, Na, Ga, and La in Mg_2Sn.

14) Yoshihiro Nagaoka *et al*.,(2014) (Ce^{3+}, Tb^{3+}) codoped NaCl phosphor is synthesized from an aqueous solution of NaCl–$CeCl_3$–$TbCl_3$. The synthesized phosphor is investigated using X-ray diffraction analysis, electron probe microanalysis, diffuse reflectance measurements, photoluminescence (PL) analysis, PL excitation spectroscopy, and PL decay measurements. The (Ce^{3+}, Tb^{3+})-codoped NaCl phosphor shows a strong Tb^{3+}related emission in the 480–690 nm spectral region, together with a very weak Ce^{3+}related emission at ∼400 nm. The Tb^{3+}related emission intensity in the codoped phosphor is enhanced more than 500 times compared to the Tb^{3+} singly doped phosphor. The enhanced emission intensity in the codoped phosphor could be attributed to an efficient energy transfer from Ce3+ to Tb3+. The maximum transfer efficiency is found to be $\eta \sim 95\%$ for the phosphor synthesized at a solution of NaCl : $CeCl_3$: $TbCl_3$ = 1 : 0.1 : 0.01 in molar ratio. The PL decay times are ∼20 ns and ∼0.4–1 ms for the Ce^{3+} and Tb^{3+} emissions, respectively. The temperature dependence of the Tb^{3+}related emission intensity yielded quenching energies of ∼50 meV and ∼0.40 eV below and above ∼300 K, respectively.

15) Lichao Zhang *et al*.,(2014) A new type of Ti/SnO_2-Sb electrode modified with carbon nanotube (CNT) has been fabricated using a pulse electrode position method. The electrode modified with CNT versus without CNT has larger surface area and smaller crystallite particles (41.9 nm versus 46.8 nm) as seen by scanning electron microscopy (SEM), and calculated through X-ray diffraction (XRD), respectively. It means that the CNT-modified electrode can provide more active sites for electrochemical oxidation of organic pollutants. Oxygen evolution potential of the CNT-modified electrode has 0.07 V higher over potential in the linear sweep voltammetry (LSV) curve. The service lifetime of Ti/SnO_2-Sb-CNT electrode is 4.8 times longer than that of the Ti/SnO_2-Sb electrode without CNT modifying. The Ti/SnO_2-Sb-CNT electrode is demonstrated to have a superior electrochemical oxidation and degradation abilities using Acid Red 73 (AR 73) as a model organic pollutant. The CNT-modified electrode has higher kinetic rate constant, chemical oxygen demand (COD) and total organic carbon (TOC) removals, and mineralization current efficiency, which is 1.93, 1.27, 1.26, and1.38 times those of the Ti/SnO_2-Sb electrode, respectively. The repeated experiments prove the reproducibility of the data. Ti/SnO_2-Sb-CNT electrode is 1.15 times more effective in permeation flux than the Ti/SnO_2-Sb electrode when combining electro-catalytic oxidation and nano filtration for treating dye wastewater.

16) Anxiang Wang *et al*., (2014) the vapor liquid phase equilibrium of Sn-Sb alloy is calculated by the molecular interaction volume model(MIVM), which is used to predict the element distribution of Sn- Sb alloy between vapor and liquid phase during vacuum distillation. In this central composite design (CCD) is used to optimize the process parameters influencing the content of Sn in liquid phase and the direct yield of Sn. Distillation temperature, feeding materials and soaking time are the studied parameters. Two quadratic mathematical model equations are derived for predicting the content of Sn in liquid phase and the direct yield of Sn. The analysis of variance (ANOVA) shows that distillation temperature is the most significant factor affecting the separation of Sn- Sb alloy. In the process optimization, while the direct yield of Sn equal to 92%, the maximum content of Sn in liquid phase should be 99.66 wt.% under the conditions of 1531 K, 137 g and 46 min. The confirmation test values of 91.22% and 99.43 wt.% are fair agreement with the predicted data, which demonstrated that this models are very good and can be used for parameter optimization in vacuum distillation.

17) Loic Baggetto *et al*.,(2014) The electrochemical reaction of Sb and SnSb anodes with Na results in the formation of amorphous materials. To understand the resulting phases and electrochemical capacities have studied the local order using ^{119}Sn and ^{121}Sb Mossbauer spectroscopies in conjunction with measurements performed on model powder compounds of

Na-Sn and Na-Sb to further clarify the reactions steps. For pure Sb the sodiation starts with the formation of an amorphous phase composed of atomic environments similar to those found in NaSb, and proceeds further by the formation of crystalline Na_3Sb. The reversible reaction takes place during a large portion of the charge process. At full charge the anode material still contains a substantial fraction of Na, explaining the lack of recrystallization into crystalline Sb. The reaction of SnSb yields Na_3Sb at full discharge at higher temperatures (65 and 95 ^0C) while the RT reaction yields amorphous compounds. The electrochemically driven, solid-state amorphization reaction occurring at RT is governed by the simultaneous formation of Na coordinated Sn and Sb environments, as monitored by the decrease (increase) of the 119_{Sn} (121_{Sb}) Mossbauer isomer shifts. Overall, the monitoring of the hyperfine parameters enables to correlate changes in Na content to the local chemical environments.

18) Jianyin Zhang *et al*.,(2014) Porous Sn/SnSb negative electrodes for lithium ion batteries are directly prepared by electro reduction of the SnO_2–$Sb2O_3$ (molar ratio = 4:1) composite electrodes in 1 mol/L H_2SO_4. After the reduction, the original dense SnO_2–$Sb2O_3$ composite electrode changed into a porous structure with the oxides almost completely reduced to nanoparticles of Sn and SnSb alloy. As the precursor electrode shows very poor electrochemical performances in lithium ion batteries, the resultant metallic porous Sn/SnSb electrode exhibited high charge capacity (800 mAh/g) and good cycling stability (70% of capacity retention at the 40th cycle) between 0.02 and 1.5 V (vs. Li/Li+) at a current density of 100 mA/g. More porous Sn/SnSb electrode is derived from the SnO_2–$Sb2O_3$ composite precursor using pore forming by NH_4HCO_3 (15 vol.%), showing enhanced electrochemical performances with an initial capacity of 900 mAh/g at 100 mA/g, and 520 mAh/g at 1 A/g at the 40th charging–discharging cycle.

19)Lingxin Kong *et al*.,(2014) Based on the molecular interaction volume model (MIVM), the pair-potential energy parameters Bji and Bij of the related binary Sn–Pb, Pb–Sb and Sn–Sb alloy systems are calculated using the infinite dilution activity coefficients γ_i^∞ and γ_j^∞. The activities of components of the Sn–Pb–Sb ternary alloy system are predicted using Bji and Bij. Finally, the vapor–liquid phase equilibrium of the Sn–Pb–Sb alloy system is predicted using only the properties of pure components and the activity coefficients, which indicates that Sn can be separated from Pb and Sb by vacuum distillation thoroughly. A significant advantage of the model lies in its ability to predict the thermodynamic properties of multi-component liquid alloys using only two parameters. The MIVM is reliable due to it has certain physical meaning from the viewpoint of statistical thermodynamics.

20) P.Nithyadharseni *et al*.,(2014) Influence of incorporating transition metal impurities such as Fe, Co and Ni on the magnetic and electrical properties of SnSb alloy nanopowders synthesized by reductive co-precipitation is reported. Structural elucidation of all the samples by X-ray diffraction (XRD) confirms hexagonal structure and the morphological observations through scanning electron microscope (SEM) show a minimal particle size of 20 nm for the Co substituted SnSb sample, among all the other impurity incorporated samples. Compositional confirmation of Sn, Sb, Fe, Co, and Ni is made using EDAX. The X-ray photoelectron spectroscopy (XPS) is used to investigate the surface of SnSb and the change in surface activity due to the addition of transition metal impurities. The magnetic hysteresis studies indicate that SnSb and SnSb:Ni exhibit diamagnetic behaviour; while the Fe and Co incorporation resulted in ferromagnetic nature. The conductivity of SnSb:Fe, SnSb:Ni shows a semiconducting nature with negative temperature coefficient of resistance; whereas pure and Co substitution exhibit metallic behaviour with positive temperature coefficient of resistance. The switching of metallic to semiconducting regime is explained in this paper.

21) Xiaoxei Zhao *et al*.,(2015) have construct successfully a porous antimony-doped tin oxide (ATO)/nitrogen-doped graphene 3-dimensional (3D) frameworks (denoted as ATO/NG/TEPA; TEPA refers to tetraethylenepentamine) by a one-pot hydrothermal process, with which TEPA aqueous solution is adopted to easily re-disperse commercial ATO precursor forming a transparent hydrosol. The results show that TEPA plays a key role in the construction of ATO/NG/TEPA, not only acting as a peptization reagent to re-disperse ATO precursor nanoparticles, and as a linker to combine ATO with graphene sheets. The as-fabricated ATO/NG/TEPA hybrid as the negative electrode of lithium ion batteries exhibits excellent lithium storage capacity and cycling stability. With the advantage of easily re-dispersing commercial ATO, the present synthetic route may be put into use for the large-scale production of the titled nano composites as the anode material of lithium ion batteries.

22)Li Xu *et al*.,(2015) Novel Ti/Cu-NRs/SnO2-Sb electrode modified by copper (Cu) nanorods was fabricated through anodic aluminum oxide (AAO) template assisted electrochemical deposition (ECD) for wastewater treatment. Scanning electron microscopy (SEM), energy dispersive X-ray (EDX), X-ray diffraction (XRD) and electrochemical methods such as linear sweep voltammetry (LSV), cyclic voltammetry (CV) and electrochemical impedance spectroscopy (EIS) are used to characterize the surface morphology, crystal structure and electrochemical performance of the electrodes. Acid dye AR 73 is selected as target pollutants to investigate the electro-catalyst behavior, and UV vs spectroscopy is used to monitor the concentration changes with time. The results indicated that the presence of Cu nanorods on the Ti substrate promoted the electrodes property obviously. Ti/Cu-NRs/SnO_2-Sb anode possessed smaller charge transfer resistance and longer service life than Ti/SnO_2-Sb anode. The oxygen evolution potential (OEP) of Ti/Cu-NRs/SnO_2-Sb electrodes reach 2.17 V (vs. Ag/AgCl). Removal of pollutants and reaction rate were all promoted due to the introduction of Cu nanorods in the process of AR 73 decomposing with Ti/Cu-NRs/SnO_2-Sb electrodes. And specific energy consumption also reduced remarkably. Their study has shown that the fabricated Ti/Cu-NRs/SnO2-Sb electrodes are very promising for the electrochemical treatment of wastewater.

23) Samuel Taub *et al*.,(2014) have studied the formation energy and atomic structure of impurities in Mg2Sn using first-principles plane-wave total energy calculations. Twenty elements, namely H, Li, Na, K, Rb, Sc, Y, La, Cu, Ag, Au, B, Al, Ga, In, N, P, As, Sb, and Bi, are selected as the impurity species. They considered structural relaxation of the atoms within the second nearest neighbors of the impurity atom in the 48-atoms upper cell. The results of the formation energy calculations suggested that Sc, Y, La, P, As, Sb, and Bi are good n-type dopants whereas Li and Na are good p-type dopants. The electrical properties of Li-,Na-,and Ga-doped Mg_2Sn and La-dopedMg_2(Si, Sn) composites reported previously can be explained by the low formation energies of Li, Na, Ga, and La in Mg_2Sn.

24) Zhaolin Na *et al*.,(2015) A novel cerium lead redox flow battery (RFB) employing Ce(IV)/Ce(III) and Pb(II)/Pb redox couples in the supporting electrolyte of methane sulfonic acid (MSA) is developed and preliminarily investigated. The RFB requires no additional catalyst and uses kinetically favorable reactions between low-cost reactants, and provides a desirable discharge voltage of approximately 1.7 V, with high average coulombic efficiency (CE) of 92% and energy efficiency (EE) of 86% over 800 cycles at 298 K. Stable cycling with an acceptable performance is achieved for a board operating temperature range of 253 K-313 K. The excellent performance obtained from the preliminary study suggests that the cerium lead RFB promises to be applicable to large-scale energy storage for electricity grids.

25) M.Mohedano *et al.*,(2015) Environmentally friendly Ce-based sealing post-treatments are developed for PEO coatings on AM50 magnesium alloy. The influence of the $Ce(NO_3)_3$ concentration in the Ce bath and the time of the sealing process are evaluated in terms of morphological and structural properties using SEM, EDS and XRD. Ce content in the layer increased with both the amount of salt in the solution and the time of the sealing post-treatment process due to a higher Ce product accumulation into the pores and cracks of the coatings. Sealed PEO coatings revealed an improvement in the corrosion protection properties as measured by electrochemical impedance spectroscopy. Differences in the corrosion resistance values for the sealed coatings indicate a strong relation between the parameters of the sealing process and its effectiveness, shows higher resistance for the sealed PEO coating developed after 3 h of immersion in 10 g/l $Ce(NO_3)_3$ sealing bath.

26) Guiling Wang *et al.*,(2015) Cerium-doped nanosheet-based porous δ-MnO_2 microspheres have been successfully prepared via a simple hydrothermal process. Electrochemical measurements shows that appropriate amount of cerium doping can significantly increase the specific capacitance of δ-MnO_2. It is found that 1.5% cerium doped manganese oxides exhibit the best specific capacitance of 382.38 Fg^{-1} at a current density of 1 Ag^{-1}. In terms of ion transport kinetics, cerium doping can shorten the diffusion path length and increase the ion transfer rate by changing the partial size, porosity density and conductivity of manganese oxides materials.

27) Hussein Hammoud *et al.*,(2015) This work presents the experimental determination of the thermal and dielectric properties of conventionally sintered cerium dioxide(CeO_2) samples, with a porosity ranging from3.68 upto 44.33 vol%. The thermal conductivity, the thermal diffusivity and the heat capacity is determined using Laser Flash analysis and Differential Scanning Calorimetry. A cylindrical micro wave cavity is developed to measure dielectric properties upto1000 ˚C. There real imaginary parts of the relative dielectric permittivity; ε^{1}_{r} and ε^{11}_{r} the dielectric loss factor, are obtained using the cavity perturbation theory inTM012 mode at 2.45GHz. These parameter scan be used as inputs for coupled thermo-mechano-electro magnetic modeling of Ceria sintering.

28) HE Wen *et al*.,(2015) Tungsten powders and Ce doped powders are prepared by hydrogen reduction combined with the liquid-solid doping method. The phase composition, particle size and powder morphology of Ce doped tungsten powders are analyzed by X-ray diffraction, scanning electron microscopy and transmission electron microscopy, respectively. The results indicated that 10000 ppm Ce doped tungsten oxide powders are consisted of WO_3 phase and $Ce_4W_9O_{33}$ phase. The hydrogen reduction of Ce doped tungsten powders is basically accomplished at 800 ºC for 3 h. The size of Ce doped W powders was remarkably decreased compared to the undoped W powders. The phase of $Ce_4W_9O_{33}$ is reduced to Ce_2 $(WO_4)_3$ phase and $Ce_2W_2O_9$ phase during the process of hydrogen reduction. Moreover, Ce_2 $(WO_4)_3$ phase and $Ce_2W_2O_9$ phase are observed form their morphologies, where the doping content of Ce is more than 100 ppm. The ternary phase embedding into W particles is assigned to $Ce_2(WO_4)_3$, while the ternary phase distributing among W particles corresponded to $Ce_2W_2O_9$. The phase of Ce_2 $(WO_4)_3$ might be the nucleus of W particles and increase the number of the nucleus. And the particles of $Ce_2W_2O_9$ covered WO_2 particles and might inhibit the growth of W particles. These two reasons resulted in the decrease of the size of Ce doped W particles. Uniform fine W powders are fabricated with the doping content of Ce more than 100 ppm.

29) M.Krawczyk *et al*.,(2015) Electron transport properties in CeO_2powder samples are studied by elastic-peak electron spectroscopy(EPES). Prior to EPES measurements, the CeO_2sample surface is pre-sputtered by 0.5 keV Ar ion etching. As a result, an altered layer with thickness of 1.3 nm is created. X-ray photoelectron spectroscopy (XPS) analysis revealed two chemical states of cerium Ce4+(68%) and Ce3+(32%) at the surface region of CeO_2sample after such treatment. The inelastic mean free path (IMFP), characterizing electron transport, is evaluated as a function of energy within the 0.5–2 keV range. Experimental IMFPs are corrected for surface excitations and approximated by the simple function $\lambda = kE^p$, where λ is the IMFP, E denoted the energy (in eV), and k = 0.207 and p = 0.6343 are the fitted parameters. The IMFPs measured here are compared with IMFPs resulting from the TPP-2M predictive equation for the measured composition of oxide surface. The measured IMFPs are found to be from 3.1% to 20.3% smaller than the IMFPs obtained from the predictive formula in the energy range of 0.5–2 keV. The EPES IMFP value at 500 eV is related to the altered layer of sputtered CeO_2samples.

30) Mariana Marino *et al*.,(2015) In single-chamber solid oxide fuel cells (SC-SOFC), anode and cathode are placed in a gas chamber where they are exposed to a fuel/air mixture. Similarly to conventional dual-chamber SOFC, the anode and the cathode are separated by an electrolyte. However, as in the SC-SOFC configuration the electrolyte does not play tightness role between compartments, this one can be a porous layer. Nevertheless, it is necessary to have a diffusion barrier to prevent the transportation of hydrogen produced locally at the anode to the cathode that reduces fuel cell performances. This study aims to obtain directly a diffusion barrier through the surface densification of the electrolyte $Ce_{0.9}Gd_{0.1}O_{1.95}$(CGO) by a laser treatment. KrF excimer laser and Yb fiber laser irradiations are used at different fluences and number of pulses to modify the density of the electrolyte coating. Microstructural characterizations confirmed the modifications on the surface of the electrolyte for appropriate experimental conditions shows either grain growth or densified but cracked surfaces. Gas permeation and electrical conductivities of the modified electrolyte are evaluated. Finally SC-SOFC performances are improved for the cells presenting grain growth at the electrolyte surface.

31) Jin-Chung Sin *et al*.,(2015) Cerium-doped ZnO hierarchical micro/nanospheres (Ce/ZnO) are prepared using a facile and surfactant-free chemical precipitation method. The as-synthesized products are characterized by X-ray diffraction, field-emission scanning electron microscopy, energy-dispersive X-ray spectroscopy, transmission electron microscopy, high-resolution transmission electron microscopy, X-ray photoelectron spectroscopy, UV–visible diffuse reflectance spectroscopy and photoluminescence spectroscopy. The results shows that the as-synthesized products are well-crystalline and accumulated by large amount of inter leaving nano sheets. It is also observed that the Ce doping led to red shift in the absorption band and improved the visible light absorption ability of the catalysts. Under visible light irradiation, the Ce/ZnO exhibited much higher photocatalytic activity than those of pure ZnO and commercial $TiO_2$for the degradation of phenol. The enhanced photocatalytic performance of Ce/ZnO can be attributed to the effective separation of charge carriers. Radical scavenger experiments and terephthalic acid-photoluminescence probing test revealed that hydroxyl radical played a pivotal role for the phenol degradation. Moreover, the Ce/ZnO shows no significant loss of the photocatalytic activity after four repeated degradation experiments, shows great potential for practical applications in environmental remediation.

32) HE Liying *et al*.,(2015) Nanostructured cerium oxide (CeO_2) commonly known as nanoceria is a rare earth metal oxide, which plays a technologically important role due to its versatile applications as automobile exhaust catalysts, oxide ion conductors in solid oxide fuel cells, electrode materials for gas sensors, ultraviolet absorbents and glass-polishing materials. However, nanoceria has little or weak luminescence, and therefore its uses in high-performance luminescent devices and biomedical areas are limited. In this review, they present the recent advances of nanoceria in the aspects of synthesis, luminescence and biomedical studies. The CeO_2 nanoparticles can be synthesized by solution-based methods including co-precipitation, hydrothermal, microemulsion process, sol-gel techniques, combustion reaction and so on. Achieving controlled morphologies and enhanced luminescence efficiency of nanoceria particles are quite essential for its potential energy and environment related applications. Additionally, a new frontier for nanoceria particles in biomedical research has also been opened, which involves low toxicity, retinopathy, biosensors and cancer therapy aspects. Finally, the summary and outlook on the challenges and perspectives of the nanoceria particles are proposed.

33) Vu Van Hung *et al*.,(2015) The pressure effects on thermodynamic properties as well as the structural phase transition of the rare earth metal cerium have been investigated by using the statistical moment method in quantum statistical mechanics. The analytical expressions of Helmholtz free energy, thermal expansion coefficient, and bulk modulus of a Ce have been derived. Numerical calculations of these above thermodynamic quantities give good and reasonable results comparing to experiments as well as other theoretical works. This research also proposes the efficiency of the statistical moment method for determining the relative change of the phase transition temperature of the process ɣ-Ce→δ-Ce under pressure.

34) Shunsuke Murai *et al*.,(2016) have synthesized thin films, consisting of yttrium aluminum garnet doped with Ce^{+3} (YAG:Ce),using the mist chemical vapor deposition(CVD)method, which allows the fabrication of high-quality thin films under atmospheric conditions without the use of vacuum equipment. Under a deposition rate of approximately1 μm/h, the obtained thin films had a typical thickness of 2 μm. The XRD analysis in di-cated that the thin films consisted of single-phase YAG:Ce. The Ruther ford back scattering confirmed the stoichiometry; the composition of the film is determined to be$(Y,Ce)_3Al_5O_{12}$, with a Ce content of Ce/(Y+Ce)=2.5%. The YAG: Ce thin films exhibited fluorescence due to the 5d–4f electronic transitions characteristic of Ce ions occupying the coordinated YAG lattice.

35) Hao Wu *et al*.,(2016) Cerium ion implantation is conducted to modify the surface properties of magnesium. Electrochemical polarization and immersion tests show that the corrosion resistance of the Mg samples is improved in artificial hand sweat, Ringer's solution, and complete cell culture medium (cDMEM) after Ce ion implantation with the most significant improvement observed from cDMEM. The retardation effect is attributed to the formation of a robust cerium-rich oxide layer formed by energetic ion bombardment and implantation.

2.2 REFERENCES

1.J. Schoonman, Nanoionics, Laboratory for Inorganic Chemistry, Delft Institute for Sustainable Energy, Solid State Ionics 157 (2003) 319– 326

2. Lavinia Balan, Raphael Schneider, Denis Billaud, Jacques Lambert, Jaafar Ghanbaja ,A novel solution-phase and low-temperature synthesis of SnSb nano-alloys, Volume 59, Issue 23, 2005, 2898–2902

3. J.K.O. Asante, J.J. Terblans, W.D. Roos, Segregation of Sn and Sb in a ternary Cu(1 0 0)SnSb alloy, Applied Surface Science 252 (2005) 1674–1678

4. Hong Guo, Hailei Zhao, Chaoli Yin, Weihua Qiu, Si/SnSb alloy composite as high capacity anode materials for Li-ion batteries, Volume 426, Issues 1–2 (2006) Pages 277–280

5. Ge Zhang, Kelong Huang, Suqin Liu, Wei Zhang, Benli Gong , Comparison of the electrochemical performance of mesoscopic Cu_2Sb, SnSb and Sn/SnSb alloy powders, Volume 426, Issues 1–2, (2006) Pages 432–437

6. Jyh-Ming Wu, Characterizing and comparing the cathodoluminesence and field emission properties of Sb doped SnO2 and SnO2 nanowires, Thin Solid Films 517 (2008) 1289–1293

7. L.K. Dua, A. De1, S. Chakraborty, P.K. Biswas, Study of spin coated high antimony content Sn–Sb oxide films on silica glass, Sol–Gel Division, Materials characterization 59 (2008)578 – 586

8. NavidaNasir , AndriyGrytsiv , PeterRogl, AdrianaSaccone , GeraldGiester, Phase equilibriain systemsCe–M–Sb (M ¼ Si, Ge,Sn)and superstructure $Ce_{12}Ge_{9-x}Sb_{23+x}$ (x = 3.8 +0.1), Journal of Solid State Chemistry 182 (2009) 645–656

9. Fei Wang, Mingshu Zhao, Xiaoping Song, The improved electrochemical performance of SnSb-based alloy anode materials for Li-ion batteries, Journal of Alloys and Compounds, Volume 472, Issues 1–2, (2009) 55–58

10. Lili Gao , Songbai Xue , Liang Zhang , Zhong Sheng , Feng Ji , Wei Dai , Sheng-lin Yu , Guang Zeng , Effect of alloying elements on properties and microstructures of SnAgCu solders, Microelectronic Engineering 87 (2010) 2025–2034

11. Sonia Rodriguez-Liviano, Francisco J. Aparicio, Teresa C. Rojas, Ana B. Hungría, Lidia E. Chinchilla, and Manuel Ocaña, Microwave-Assisted Synthesis and Luminescence of Mesoporous RE Doped YPO4 (RE = Eu, Ce, Tb, and Ce + Tb) Nanophosphors with Lenticular Shape, pubs.acs.org/crystal.

12. Feng Dan Wu, Minghong Wu, Yong Wang, Antimony-doped tin oxide nanotubes for high capacity lithium storage, Electrochemistry Communications 13 (2011) 433–436

13.Jun-ichi Tani n, HiroyasuKido, Impurity dopingintoMg2Sn: A first-principles study, Physica B 407 (2012) 3493–3498

14. Yoshihiro Nagaoka and Sadao Adachi , High Energy Transfer Efficiency in Photoluminescence of (Ce3+, Tb3+)-Codoped NaCl Green Phosphor, ECS Journal of Solid State Science and Technology, **3** (4) R43-R49 (2014)

15. Lichao Zhang, Li Xua, Jing He, Jiejing Zhang, Preparation of Ti/SnO2-Sb electrodes modified by carbon nanotube for anodic oxidation of dye wastewater and combination with nanofiltration, Electrochimica Acta 117 (2014) 192– 201

16. Anxiang Wang , Yifu Li , Bin Yang , Baoqiang Xu , Lingxin Kong , Dachun Liu , Process optimization for vacuum distillation of Sn-Sb alloy by response surface methodology, Vacuum 109 (2014) 127-134

17. Loic Baggetto , Hien-Yoong Hah , Jean-Claude Jumas , Charles E. Johnson ,Jacqueline A. Johnson , Jong K. Keum , Craig A. Bridges , Gabriel M. Veith , The reaction mechanism of SnSb and Sb thin film anodes for Na-ion batteries studied by X-ray diffraction, ^{119}Sn and ^{121}Sb Mossbauer spectroscopies, Journal of Power Sources 267 (2014) 329-336

18. Jianyin Zhang , Zhiyong Wang , Yanzhong Hong , Shengxian Li , Xianbo Jin , George Z. Chen, Electrochemical fabrication of porous Sn/SnSb negative electrodes from mixed SnO_2–Sb_2O_3, Electrochemistry Communications 38 (2014) 36–39

19. Lingxin Kong, Bin Yang,Baoqiang Xu, Yifu Li, Dachun Liu,Yongnian Dai, Application of MIVM for phase equilibrium of Sn–Pb–Sb system in vacuum distillation, Fluid Phase Equilibria 364 (2014) 1– 5

20. P.Nithyadharseni, B.Nalini, P.Saravanan, Electrical and magnetic effect of transition metals in SnSb nanoalloy, Applied Surface Science, Volume 311, 30 August 2014, Pages 503–507

21. Xiaowei Zhao , Jingwei Zhang , Jiwei Zhang , Chunhong Gong ,Xiufang Gu , Zhihua Ma , Jingfang Zhou , Laigui Yu , Zhijun Zhang , Construction of spongy antimony-doped tin oxide/grapheme nanocomposites using commercially available products and its excellent electrochemical performance, Journal of Power Sources 294 (2015) 223-231

22. Li Xu , Ming Li , Wei Xu, Preparation and characterization of Ti/SnO2-Sb electrode with copper nanorods for AR 73 removal, Electrochimica Acta 166 (2015) 64–72

23. Samuel Taub , Robert E.A. Williams , Xin Wang , David W. McComb , John A. Kilner ,Alan Atkinson, The effects of transition metal oxide doping on the sintering of cerium gadolinium oxide, Acta Materialia 81 (2014) 128–140

24. Zhaolin Na , Shengnan Xu , Dongming Yin , Limin Wang , A cerium lead redox flow battery system employing supporting electrolyte of methane sulfonic acid, Journal of Power Sources 295 (2015) 28-32

25. M. Mohedano , C. Blawert, M.L. Zheludkevich, Cerium-based sealing of PEO coated AM50 magnesium alloy, Surface & Coatings Technology 269 (2015) 145–154

26. Guiling Wang, Zhipeng Ma, Guowei Zhang, Chunying Li, Guangjie Shao, Cerium-doped porous K-birnessite manganese oxides microspheres as pseudocapacitor electrode material with improved electrochemical capacitance, Electrochimica Acta 182 (2015) 1070–1077

27. Hussein Hammoud, SébastienVaucher, Fran¸ oisValdivieso, Dielectric and thermal properties of cerium dioxide upto1000 °C and the effect of the porosity for microwave processing studies, Thermochimica Acta 617 (2015) 83–89

28. HE Wen , TAN Dunqiang , LI Yalei , YANG Xin, LU Lei ,LU Deping, Effect of rare earth element cerium on preparation of tungsten powders, Journal of rare earth, Vol. 33, No. 5, May 2015, P. 561

29. M. Krawczyk, M. Holdynski, W. Lisowski, J.W. Sobczak, A. Jablonski, Electron inelastic mean free paths in cerium dioxide, Applied Surface Science 341 (2015) 196–202

30. Mariana Marino, Mathilde Rieu, Jean-Paul Viricelle, Florence Garrelie, Laser induced densification of cerium gadolinium oxide: Application to single-chamber solid oxide fuel cells, Applied Surface Science (2015)

31. Jin-Chung Sin, Sze-Mun Lam, Keat-Teong Lee, Abdul Rahman Mohamed, Preparation of cerium-doped ZnO hierarchical micro/nanospheres with enhanced photocatalytic performance for phenol degradation under visible light , Journal of Molecular Catalysis A: Chemical 409 (2015) 1–10

32. HE Liying , SU Yumin , Jiang Lanhong, SHI Shikao , Recent advances of cerium oxide nanoparticles in synthesis, luminescence and biomedical studies: a review, Journals of rare earth elements, Vol. 33, No. 8, Aug. 2015, P. 791

33. Vu Van Hung , Dang Thanh Hai , Ho Khac Hieu , Thermodynamic properties and structural phase transition of cerium under high pressure, Vacuum 114 (2015) 119-123

34. Shunsuke Murai n, TakafumiSato,SituYao,RyosukeKamakura,KojiFujita, Katsuhisa Tanaka, Fabrication of cerium-doped yttrium aluminum garnet thin films by a mist CVD method, Journal ofLuminescence170(2016)808–811

35. Hao Wu, Guosong Wu, Paul K.Chu , Effects of cerium ion implantation on the corrosion behavior of magnesium in different biological media, Surface & Coatings Technology (2016)

METHODOLOGY

CHAPTER III

SYNTHESIS AND EXPERIMENTAL TECHNIQUES

3. Introduction

This chapter describes experimental techniques used in the preparation and characterization of rare earth element Ce (Cerium) doped SnSb alloy. Cerium is the most abundant rare earth metal in the earth's crust. The method of preparation used in this study to prepare SnSb doped with Cerium is co-precipitation technique. The various experimental techniques such as X-ray Diffraction (XRD) for the structural analysis, Scanning Electron Microscope (SEM) for Morphological analysis, Fourier Transform Infrared Spectroscopy (FTIR) for the analysis of atomic environment through bond vibrations and Photo luminescence (PL) studies for the understanding of electronic energy level available for charge transfer have been employed in these samples for better understanding of this SnSb alloy.

3.1 Experimental Procedure:

The raw materials chosen are

- Tin chloride ($SnCl_2$)
- Antimony chloride ($SbCl_3$)
- Trisodium citrate ($Na_3C_6H_5O_7$)
- Cerium chloride ($CeCl_3$)
- Sodium hydroxide (NaOH)
- Sodium borohydride ($NaBH_4$)

The raw materials are taken in appropriate gram molecular weights and dissolved in 50ml distilled water. The two solutions, later two in a separate solution, are stirred for 30min and 20 minutes separately and mixed to each other dropwise until precipitate forms. The precipitate thus formed is washed thoroughly with dilute HCl, Water and acetone for several times to remove residual chlorine in the precipitate.

3.2 Structural and Morphology studies

3.2.1 X-Ray Diffraction (XRD)

XRD is a nondestructive technique to identify crystalline phases, orientation, measure atomic arrangement and determine structural properties such as, lattice parameters, strain, grain size, expitaxy, phase composition, preferred orientation order-disorder transformation, thermal expansion). X-ray diffraction technique is based on the analysis of the interference of a monochromatic beam of x-rays scattered at angles from each set of lattice planes in a sample. The peak intensities are determined by the specified atoms in the lattice. XRD is a fingerprint of a periodic arrangement of atoms in a material. The data peaks are identified using JCPDS data through which crystalline structure h,k,l values can be identified.[1]

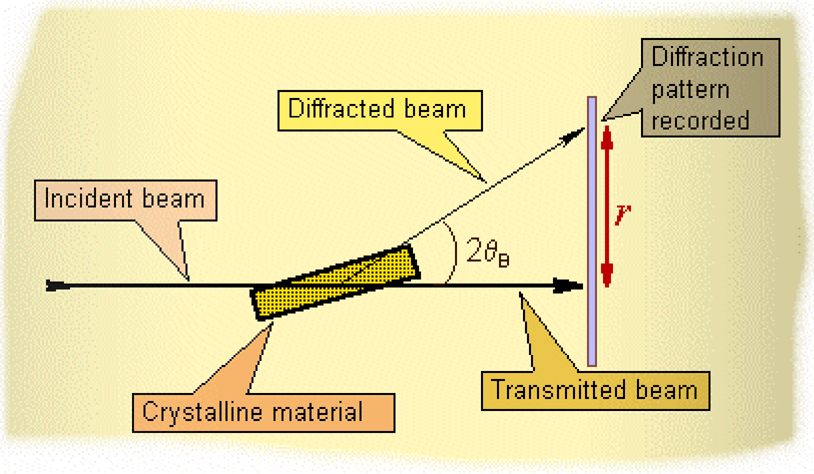

Figure 3.1 Schematic of X ray diffraction technique

Samples

The X-ray diffraction is mainly used for "finger print identification" of various solid materials. Normally the sample is ground down to particles of about 0.002mm to 0.005mm cross section. The ideal sample is homogeneous and the crystallites are randomly distributed. The sample is pressed onto a sample holder to arrive at a smooth flat surface. In X-ray diffractometer, the sample holder is made of an aluminum plate.

Figure 3.2 Photograph of X-Ray Diffractometer

Only planes (h, k, l) that are parallel to the specimen surface will contribute to the reflected intensities. If the sample is truly random, each possible reflection from a given set of h, k, l planes having an equal number of crystallites contributing to it. Only have to rock the sample through the glancing angle θ in order to produce all possible reflection. The diffraction patterns are recorded and analyzed for identification; data are compared to confirm the phase formation with JCPDS (ICDD).

3.2.2 Bragg's Formula:

Bragg's law is explaining the interference pattern of X-rays scattered by crystals, diffraction has been developed to study the structure of all states of matter with any beam.

Bragg's law,

$$n\lambda=2d\sin\theta$$

where ,

d is the distance between atomic layers in a crystal

λ is the wavelength of the incident X-ray beam

X-ray diffraction (XRD) is the direct evidence for the periodic atomic structure of crystals.

3.2.3 Scherrer's Formula

If there is no homogeneous strain, the crystallite size, D, can be estimated from the peak width with the Scherrer's formula [2],

$$\mathbf{D = k \lambda / \beta \cos \theta}$$

Where,

λ is the x-ray wavelength

β is the full width of height maximum (FWHM) of a diffraction peak,

θ is the diffraction angle,

k is the Scherrer's constant of the order of unity.

In addition, X-ray diffraction only provides the collective information of the particle sizes and usually requires a sizeable amount of powder. This technique is very useful in characterizing nanoparticles. The film thickness of epitaxial and highly textured thin films can also be estimated with X-ray diffraction [3].

3.3 FT-IR Spectroscopy:

FT-IR stands for Fourier Transform Infra-Red, the preferred method of infrared spectroscopy. In infrared spectroscopy, IR radiation is passed through a sample. Some of the infrared radiation is absorbed by the sample and some of the radiation is transmitted. The resulting spectrum represents the molecular absorption and transmission, creating a molecular fingerprint of the sample. No two unique molecular structures produce the same infrared spectrum and hence are referred as fingerprints. This makes infrared spectroscopy useful for several types of analysis.

- It can identify unknown materials
- It can determine the quality or consistency of a sample
- It can determine the amount of components in a mixture

Infrared spectroscopy has been a workhorse technique for material analysis in the laboratory. An infrared spectrum represents a fingerprint of a sample with absorption peaks which correspond to the frequencies of vibrations between the bonds of the atoms making up the material.

Because each different material is a unique combination of atoms, no two compounds produce the exact same infrared spectrum. Therefore, infrared spectroscopy can result in a positive identification (qualitative analysis) of every different kind of material. In addition, the size of the peaks in the spectrum is a direct indication of the amount of material present. With modern software algorithms, infrared is an excellent tool for quantitative analysis. The original infrared instruments are of the dispersive type. These instruments separated the individual frequencies of energy emitted from the infrared source. This is accomplished by the use of a prism or grating. An infrared prism works exactly the same as a visible prism which separates visible light into its colors (frequencies). A grating is a more modern dispersive element which better separates the frequencies of infrared energy. The detector measures the amount of energy at each frequency which has passed through the sample. This results in a spectrum which is a plot of intensity vs. frequency.

Fourier transform infrared spectroscopy is preferred over dispersive or filter methods of infrared spectral analysis for several reasons:

- It is a non-destructive technique
- It provides a precise measurement method which requires no external calibration
- It can increase speed, collecting a scan every second
- It has greater optical throughput
- It is mechanically simple with only one movie part

3.3.1 Instrumentation:

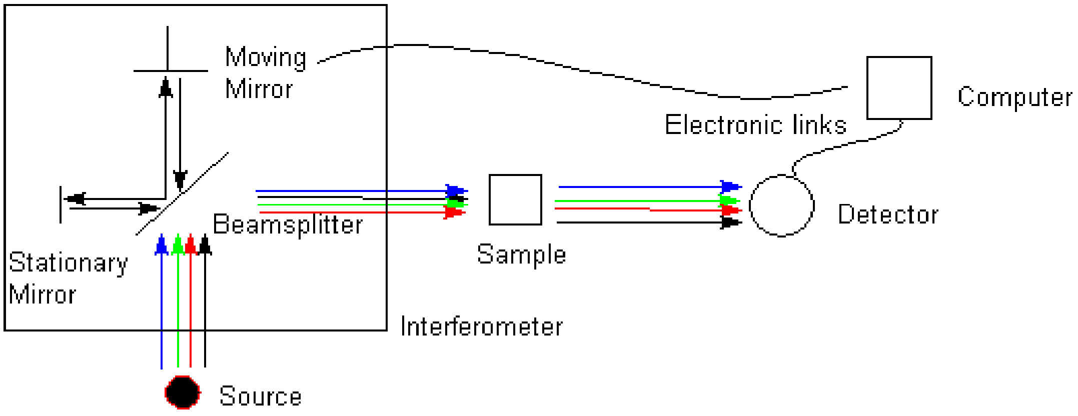

3.3 Michelson Interferometer

An FT-IR is typically based on a Michelson Interferometer. It consists of source, a sample and a detector. All the source energy is sent through an interferometer and onto the sample. In every scan, all source radiation gets to the sample. The interferometer is fundamentally a different piece of equipment than a monochromator. The light passes through a beam splitter, which sends the light in two directions at right angles. One beam goes to a stationary mirror then back to the beam splitter. The other goes to a moving mirror. The motion of the mirror makes the total path length variable versus that taken by the stationary-mirror beam. When the two meet up again at the beam splitter, they recombine, but the difference in path lengths creates constructive and destructive interference resulting in an interferogram.

The recombined beam passes through the sample. The sample absorbs all the different wavelengths characteristic of its spectrum, and this subtracts specific wavelengths from the interferogram. The detector reports variation in energy versus time for all wavelengths simultaneously. A laser beam is superimposed to provide a reference for the instrument operation.

3.3.2 Instrumental process:

Source: Infrared energy is emitted from a glowing black-body source. This beam passes through an aperture which controls the amount of energy presented to the sample.

Interferometer: The beam enters the interferometer where the "spectral encoding" takes place. The resulting interferogram signal then exits the interferometer.

Sample: The beam enters the sample compartment where it is transmitted through or reflected off of the surface of the sample, depending on the type of analysis being accomplished. This is where specific frequencies of energy, which are uniquely characteristic of the sample, are absorbed.

Detector: The beam finally passes to the detector for final measurement. The detectors used are specially designed to measure the special interferogram signal.

Computer: The measured signal is digitized and sent to the computer where the Fourier Transformation takes place. Finally we got the infrared spectrum.

3.3.3 Advantages:

Speed: The frequencies are measured simultaneously.

Sensitivity: Sensitivity is dramatically improved with FT-IR for many reasons. The detectors employed are much more sensitive, the optical throughput is much higher (referred to as the

Jacquinot Advantage) which results in much lower noise levels, and the fast scans enable the co-addition of several scans in order to reduce the random measurement noise to any desired level (referred to as signal averaging).

Mechanical Simplicity: The moving mirror in the interferometer is the only continuously moving part in the instrument. Thus, there is very little possibility of mechanical breakdown.

Internally Calibrated: These instruments employ a He-Ne laser as an internal wavelength calibration standard (referred to as the Connes Advantage). These instruments are self-calibrating and never need to be calibrated by the user. These advantages, along with several others, make measurements made by FT-IR extremely accurate and reproducible. This is the very reliable technique for positive identification of virtually any sample. The sensitivity benefits enable identification of even the smallest of contaminants. This makes FT-IR an invaluable tool for quality control or quality assurance applications whether it is batch-to-batch comparisons to quality standards or analysis of an unknown contaminant. In addition, the sensitivity and accuracy of FT-IR detectors, along with a wide variety of software algorithms, have dramatically increased the practical use of infrared for quantitative analysis. Quantitative methods can be easily developed and calibrated and can be incorporated into simple procedures for routine analysis. Thus, the Fourier Transform Infrared (FT-IR) technique has brought significant practical advantages to infrared spectroscopy. It has made possible the development of many new sampling techniques which were designed to tackle challenging problems which were impossible by older technology. It has made the use of infrared analysis virtually limitless.

3.4 Ultra-Violet Spectroscopy:

Ultraviolet–visible spectroscopy or ultraviolet-visible spectrophotometry (**UV-Vis** or **UV/Vis**) refers to absorption spectroscopy or reflectance spectroscopy in the ultraviolet-visible spectral region. This means it uses light in the visible and adjacent (near-UV and near-infrared [NIR]) ranges. The absorption or reflectance in the visible range directly affects the perceived color of the chemicals involved. In this region of the electromagnetic spectrum, molecules undergo electronic transitions. This technique is complementary to fluorescence spectroscopy, in that fluorescence deals with transitions from the excited state to the ground state, while absorption measures transitions from the ground state to the excited state.

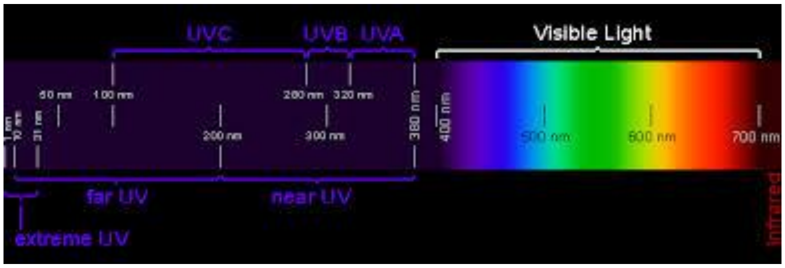

Figure 3.4Electromagnetic spectrum indicating various ranges of UV and Visible wavelengths

Principle:

Molecules containing π-electrons or non-bonding electrons (n-electrons) can absorb the energy in the form of ultraviolet or visible light to excite these electrons to higher anti-bonding molecular orbitals. The more easily the excited electrons (*i.e.* lower energy gap between the HOMO and the LUMO), the longer is the wavelength of light, it can absorb.

A beam of white lights is allowed to pass through a glass cell or cuvette filled with liquid or through the thin film of the sample to be measured, the emergent radiation has less than that entering. The decrease in power is different for different colours. The loss in power is due to reflections at the surface and also due to scattering by any suspended particles present. In the case of clear liquids, the loss is primarily due to the absorption of radiant energy by the liquid. In a solid film, the prerequisite is that the sample has to be transparent enough to measure the absorption occurring in the sample. When the sample is thin enough to transmit the incident light in intensity to illuminate the Photomultiplier tube or the detector, the absorption can be measured easily. Unlike the liquid sample, many samples are devoid of reflection.

Table 3.1 Colours of visible radiation

Approximate wavelength range, nm	Colour	Complementary Colour
400-465	Violet	Yellow-Green
465-482	Blue	Yellow
482-487	Greenish-Blue	Orange
487-493	Blue-Green	Red-Orange
493-498	Bluish-Green	Red
498-530	Green	Red-Purple
530-559	Yellowish-Green	Reddish-Purple
559-571	Yellow-Green	Purple
571-576	Greenish-Yellow	Violet
576-580	Yellow	Blue
580-587	Yellowish-Orange	Blue
587-597	Orange	Greenish-Blue
597-617	Reddish-Orange	Blue-Green
617-780	Red	Blue-Green

The range of wavelength visible to human eyes consists of electromagnetic radiations of wavelength in the region 4000-8000A^{0}and above 8000A^0 are invisible and lie in the ultraviolet (UV) and infrared (IR) regions respectively. Thus visible region is responsible for producing a definite colour to a particular substance. Light is composed of seven different colours in the visible range of wavelength namely Violet (V), Indigo (I), Blue (B), Green (G), Yellow (Y), Orange (O) and Red (R) (VIBGYOR)[5].

3.5 Photoluminescence (PL) – fluorescence spectroscopy:

Photoluminescence spectroscopy is a contactless, nondestructive method of probing the electronic structure of materials. Light is directed onto the sample, where it is absorbed and imparts excess energy into the material in the process called photo-excitation. This excess energy can be dissipated by the sample through the emission of light, or luminescence. In this case of photo excitation, this luminescence is called photoluminescence.

Photo-excitation causes electrons within a material to move into permissible excited states. When these electrons return to their equilibrium states, the excess energy is released and may include the emission of light (a radiative process) or may not (a non-radioactive process). The energy of the emitted light (photoluminescence) relates to the difference in energy levels between the two electron states involved in the transition between the excited state and the equilibrium state. The quantity of the emitted light is related to the relative contribution of the radiative process[6]. The intensity and the spectral content of the emitted photoluminescence is a direct measure of various important material properties including,

Band gap Determination: The spectral distribution of PL from a semiconductor can be analyzed to nondestructively determine the electronic bandgap. This provides a means to quantify the elemental composition of compound semiconductor and is a vitally important material parameter influencing solar cell device efficiency.

Impurity Levels and Defect Detection: The PL spectrum at low sample temperatures often reveals spectral peaks associated with impurities contained within the host material. The high sensitivity of this technique provides the potential to identify extremely low concentrations of intentional and unintentional impurities that can strongly affect material quality and device performance.

Recombination Mechanisms: The quantity of PL emitted from a material is directly related to the relative amount of radiative and non-radiactive recombination rates. Non-radiative rates are typically associated with impurities and thus, this technique can qualitatively monitor changes in material quality as a function of growth and processing conditions [7].

3.6 Jablonski Diagram

A **Jablonski diagram** is a diagram that illustrates the electronic states of a molecule and the transitions between them. The states are arranged vertically by energy and grouped horizontally by spin multiplicity. Nonradiative transitions are indicated by squiggly arrows and radiative transitions by straight arrows. The vibrational ground states of each electronic state are indicated with thick lines, the higher vibrational states with thinner lines [8]. The diagram is named after the Polish physicist Aleksander Jabłoński [9] .

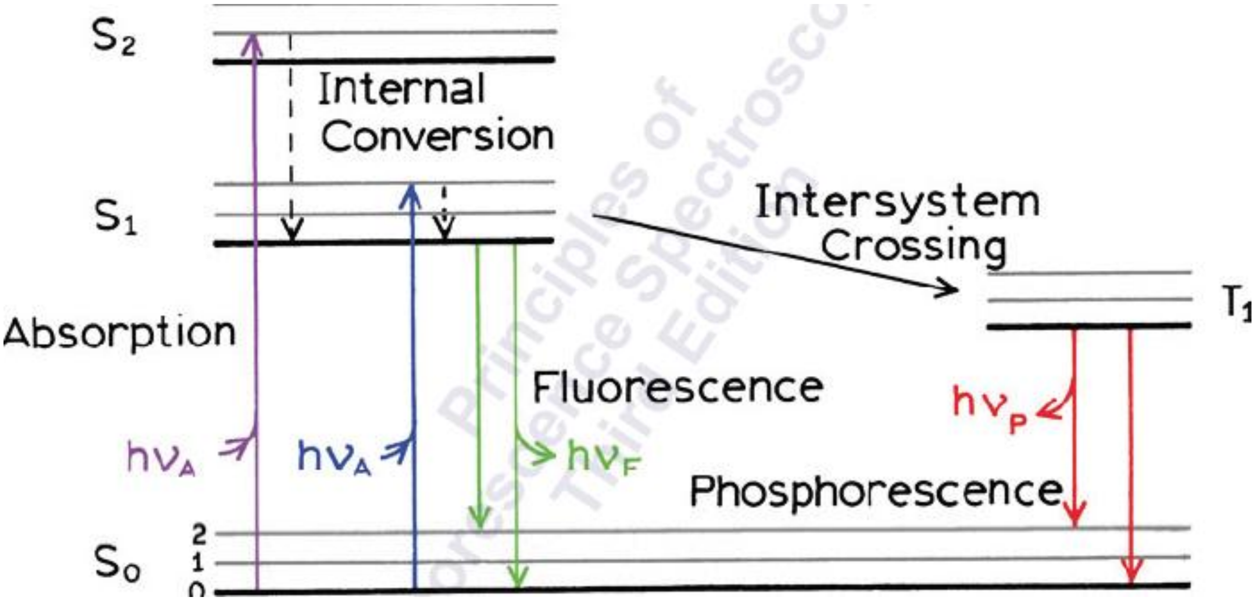

Figure 3.5 Jablonski Diagram

Jablonski diagram (3.5) is basically an energy diagram, arranged with energy on a vertical axis. The energy levels can be quantitatively denoted, but most of these diagrams use energy levels schematically. The rest of the diagram is arranged into columns. Every column usually represents a specific spin multiplicity for a particular species. However, some diagrams divide energy levels within the same spin multiplicity into different columns. Within each column, horizontal lines represent eigenstates for that particular molecule. Bold horizontal lines are representations of the limits of electronic energy states. Within each electronic energy state are multiple vibronic energy states that may be coupled with the electronic state. Usually only a portion of these vibrational eigenstates are represented due to the massive number of possible vibrations in a molecule. Each of these vibrational energy states can be subdivided even further into rotational energy levels; however, typical Jablonski diagrams omit such intense levels of detail. As electronic energy states increase, the difference in energy becomes continually less, eventually becoming a continuum that can be approach with classical mechanics. Additionally, as the electronic energy levels get closer together, the overlap of vibronic energy levels increases.

3.6.1 Transition

Radiative transitions involve the absorption, if the transition occurs to a higher energy level, or the emission, in the reverse case, of a photon. Nonradiative transitions arise through several different mechanisms, all differently labeled in the diagram. Relaxation of the excited state to its lowest vibrational level is called Vibrational relaxation. This process involves the dissipation of energy from the molecule to its surroundings, and thus it cannot occur for isolated molecules. A second type of nonradiative transition is internal conversion (IC), which occurs when a vibrational state of an electronically excited state can couple to a vibrational state of a lower electronic state. A third type is intersystem crossing (ISC); this is a transition to a state with a different spin multiplicity. In molecules with large spin-orbit coupling, intersystem crossing is much more important than in molecules that exhibit only small spin-orbit coupling. This type of nonradiative transition can give rise to phosphorescence.

The first step is the transition from higher excited singlet states to the lowest excited singlet state $S_{1.}$ This is called internal conversion (IC). It is a non radiative process and occurs in less than 10^{-11} second.

Path 1: The molecule may lose rest of the energy also in the form of heat so that the complete path is non-radiative.

Path 2: Molecule releases energy in the form of light or UV radiation. This is called Fluorescence.

Path 3: Some energy may lost in transfer from S_1 to T_2 in the form of heat. It is called intersystem crossing (ISC) and this path is non –radiative.

Path 4: After ISC, the molecule may lose of energy in the form of light in going from the excited triplet state to the ground state. This is called phosphorescence.

3.7 Reference

1. http://www.eag.com/mc/x-ray-diffraction.html
2. L.S.Birks and H.Friedman; Journal of applied Physics;17;687;1946.
3. A.Segmuller and M.Murakani;in thin films free atoms and particles,ed K.J.Klabunde;Academic Press,Orlando,FL;325;1985.
4. https://en.wikipedia.org/wiki/Scanning_electron_microscope
5. B.K.Sharma;Spectroscopy;20;S.K.Rastogim form Krishna Prakashan Media (P) Ltd.,69;2007
6. http://cnx.org/contents/gbsDEZju@2/Photoluminescence-Spectroscopy
7. http://www.nrel.gov/pv/measurements/photoluminescence_spectroscopy.html
8. Elumalai.P.,Atkins.P.,de Paula, J. Atkin’s Physical Chemistry , Oxford University Press,2002,ISBN 0-19-879285-9
9. Jablonski ,Aleksander “Efficiency of Anti-Stokes Fluorescence in Dyes” Nature 1933, volume 131, pp.839-840.doi :10.1038/131839b0

RESULT AND DISCUSSION

CHAPTER IV

RESULT AND DISCUSSION

4.1 Introduction

This chapter deals with the results of Sn_2Sb_3 and with cerium doped $Sn_{2-x}Ce_xSb_3$. Out of the various compositions where x= 0.2, 0.4 and 0.6, x=0.6 resulted in better results and hence x=0.6 is presented here.

4.2 Structural Characterization

4.2.1 X-Ray Diffraction Analysis (XRD)

The prepared Sn_2Sb_3 and $Sn_{1.4}Ce_{0.6}Sb_3$ composition doped with Cerium is investigated with X-ray Diffraction to determine the phase formation. The X-Ray diffraction pattern of SnSb doped with cerium compositions as prepared by co-precipitation method is shown in Figure 4.1. The SnSb in the composition 2:3 is doped with three compositions namely 0.2, 0.4 and 0.6 of Ce in this host lattice. The results observed for 0.6 is the best and only this composition results are presented here. In all the samples, the peaks at 28^0,41^0,42^0,51^0 and 60^0 corresponds to the (101), (012), (110), (003), and (202) for Sn_2Sb_3.

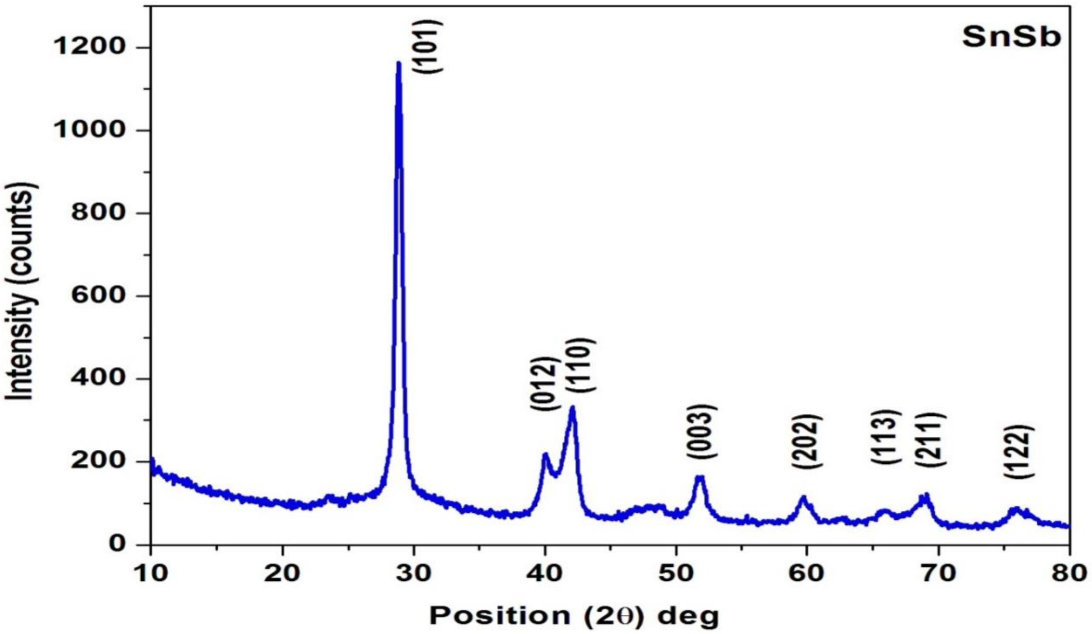

Figure 4.1 X-ray Diffractogram of the Sn_2Sb_3 alloy

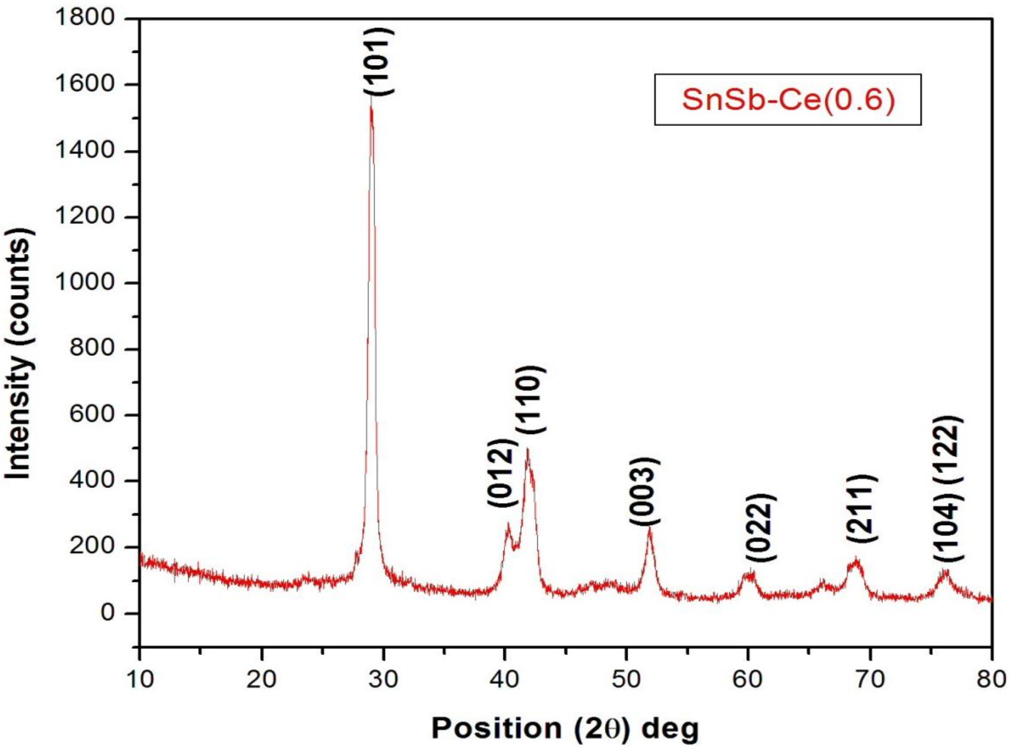

Figure 4.2 X-ray diffractogram of the $Sn_{1.4}Ce_{0.6}Sb_3$

A sharp peak obtained in XRD pattern indicates the crystallinity of the prepared samples. The XRD pattern observed for $Sn_{1.4}Ce_{0.6}Sb_3$ is not different from that of the Sn_2Sb_3. This indicates that the structure is left undisturbed by the cerium atoms in the substitution limits which are chosen in these studies. It is also to be noted that there are no new peaks observed in doped sample which is an indication of the stable crystal structure for the doped Sn_2Sb_3. The results are analyzed with the standard diffraction pattern (JCPDS card no- 33-0118) and the crystal system possesses rhombohedral structure. Due the fact that all the peaks except one at 68˚ which is assigned as (004) peak falls into the formula –h+k+l=3n which is for a hexagonal structure. Hence the structure has got rhombohedral structure falling into irregular hexagonal distribution of atoms [1]. The lattice parameter calculated is given in the Table 4.1. Compared to the JCPDS lattice parameters, there is a size reduction in “c” when “a” is maintained and when “a” is reduced “c” is blotted. But, it is to be noted that this size variation is just few 100^{th} is an angstrom and is not of much importance. The similar behavior is observed for the doped SnSb. All the remaining peaks are assigned to the corresponding (hkl) planes based on the JCPDS data as indicated in the figure 4.1 and 4.2 respectively. Crystallite size is calculated by using Debye Scherrer formula

$$\mathbf{d= 0.9\lambda/ \beta\cos(\theta)}$$

where,
d is the Crystallite size,
λ is the wavelength of the radiation (1.5405Å for Cu-Kα radiation),
β is the full width at half maximum of the peak (radians),
θ is half of the peak position (radians).

The diffraction peaks observed at 28.75^0, 40.04^0, 42.11^0, 51.87^0, 59.64^0, $66.01^{0,}$ and 68.95^0 shows a small shift in position towards the higher angle side in the doped sample compared to the undoped sample which is an indication of either the crystallite size increment and increased strain in the doped SnSb. Lattice strain value of both the samples were calculated using the formula,

$$\mathbf{\varepsilon=\beta\ Cot\ (\theta)}$$

where

ε - Strain

β-Full width at half maximum of the peak (radians)

θ- half of the peak position

The calculated values of crystallite size, lattice strain and all the other lattice parameters obtained for both the samples are listed in the table 4.2 and 4.3. The increment in crystallite size is observed for $Sn_{1.4}Ce_{0.6}Sb_3$ sample from 16 nm to 26 nm. This may be due to the higher ionic radius of Cerium (1.01Å) $Sn_{1.4}Ce_{0.6}Sb_3$ (ionic radii of Sn-0.55 Å; Sb- 0.76 Å)

Table 4.1 The different <hkl> planes assignment to the XRD peaks obtained Sn_2Sb_3; lattice constants, a= 4.428Å, c= 5.2886Å, Volume = 89.797 Å^3

No .of peaks	2θ (deg)	h	K	l	1/d^2 cal (x10^8)	FWHM	Strain
1	23.626	1	0	1	2.451	0.802	0.002
2	28.757	0	1	2	2.105	0.334	0.005
3	40.042	1	1	0	3.181	0.401	0.007
4	42.110	0	0	3	1.320	0.267	0.004
5	51.871	2	0	2	1.140	0.669	0.011
6	59.646	1	1	3	1.179	0.802	0.014
7	66.010	2	1	1	1.028	0.802	0.014
8	68.959	1	2	2	2.451	0.936	0.016

Table 4.2 The different <hkl> planes assignment to the XRD peaks obtained $Sn_{1.4}Ce_{0.6}Sb_3$; lattice constants, a= 4.335Å, c= 5.289Å, Volume = 86.095 Å^3

No .of peaks	2θ(deg)	h	k	L	1/d^2 cal (x10^8)	FWHM	Strain
1	28.93	0	1	2	3.065	0.267	0.001
2	40.32	1	1	0	1.580	0.535	0.003
3	42.31	0	0	3	2.545	0.334	0.002
4	51.85	2	0	2	3.771	0.234	0.001
5	59.67	1	1	3	1.710	0.535	0.004
6	66.08	2	1	1	1.180	0.802	0.007
7	68.36	1	2	2	1.793	0.535	0.004

4.3 Optical structure analysis

4.3.1 Fourier Transform Infrared Spectroscopy:

In the present work, the characteristic of the $Sn_{1.4}Ce_{0.6}Sb_3$ frequencies are compared. FTIR spectra of Sn_2Sb_3 and $Sn_{1.4}Ce_{0.6}Sb_3$ are recorded at room temperature in the wavelength range of 4000- 400 cm^{-1}. The range of vibrations obtained in the region of 3500-4000 cm^{-1} are attributed to the OH vibrations which may be due to the moisture content arose from the hygroscopic nature of KBr during the pelletization. Hence the spectra are presented only upto 3500cm^{-1}.The various peaks observed in the recorded region are assigned to the inter-metallic bonds[1]. Comparing the FTIR spectrum obtained for metal oxide nanoparticles, it can be claimed that pristine and doped SnSb samples are free from oxide impurities. The oxides of Sn, Sb and Ce would occur at 680 cm^{-1}, 565 cm^{-1}, 784 cm^{-1}, 866 cm^{-1} and 968 cm^{-1}[2-4].As none of these peaks are observed and hence it is assured that the alloys are devoid of oxygen in the lattice. The obtained vibrational peaks and the corresponding shift in wave numbers for doped SnSb are listed in the table 4.3. In the Cerium substituted sample, there is severe vibration at small amplitudes from 2100 to 3400cm^{-1}. The suspicion of instrumental error is ruled out as the pure sample has shown better results in this region. Hence, it is concluded that this oscillation may be due to the weak bonding of Ce and thus causing lattice loosening in the sample.

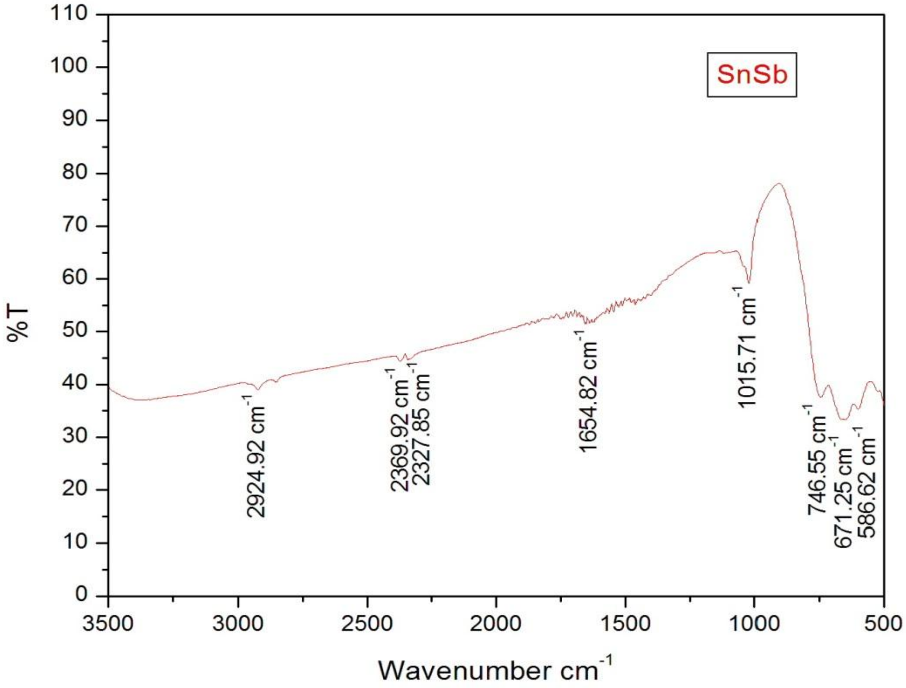

Figure 4.3 FTIR Spectrum of Sn_2Sb_3

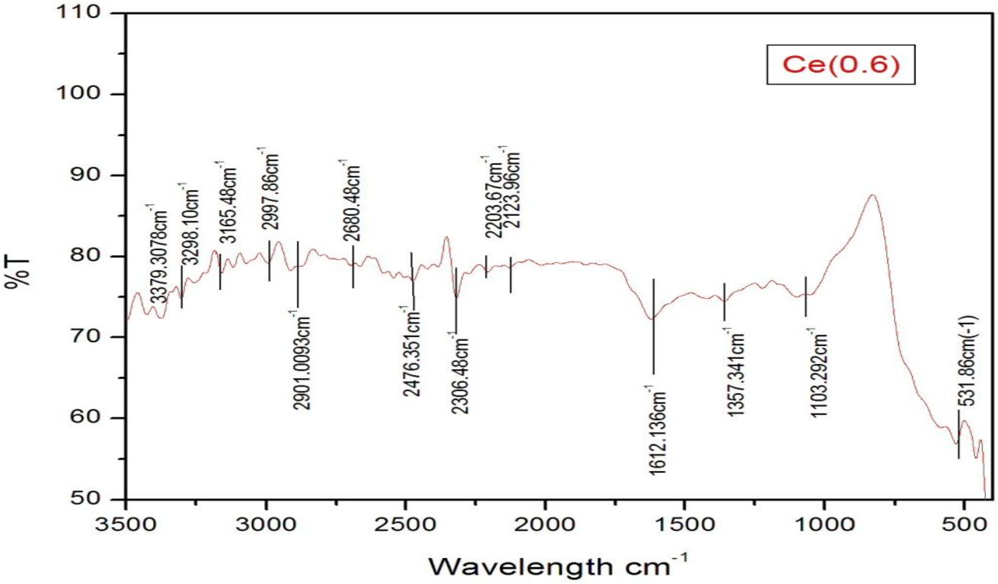

Figure 4.4 FTIR Spectrum of $Sn_{1.4}Ce_{0.6}Sb_3$

Table 4.3. Vibrational peak assignment for Sn_2Sb_3 and $Sn_{1.4}Ce_{0.6}Sb_3$

Peak no	**Sn_2Sb_3**	**$Sn_{1.4}Ce_{0.6}Sb_3$**	**peak**
1	-	458.975	Due to Ce-Sn / Ce-Sb
2	-	531.293	Due to Ce-Sn / Ce-Sb
3	1099.23	1103.292	Sn-Sb
4	1654.82	1612.136	Sn-Sb
5	2327.85	2306.48	Sn-Sb
6	2369.92	-	
7	2924.92	2997.86	Lattice loosening
8	-	3372.89	Lattice loosening

Comparing both the FTIR spectra, there is a slight shifting towards higher wavenumber for inter-metallic bond which shows that bond has altered after the addition of dopants into the pure Sn_2Sb_3. New peaks indicate that the Ce-Sn or Ce-Sb bond occurs in the structure. Altogether, it is clear that Ce has entered into the crystal structure and bonded with Sn/Sb. However, the rhombohedral structure is unaltered and this statement is validated on comparison with the XRD pattern observed for both the samples.

4.3.2 Optical Absorption studies:

Uv Vis Spectrophotometer is employed to understand the absorption profile of these samples. The absorption spectrum is obtained from 200nm to 2200nm using Jasco V600 instruments. There is a major broad absorption in the region from 300 to 800nm. Transmittance spectrum is also acquired and the tauc plot with $(\alpha h\nu)^2$ Vs $h\nu$ is plotted. The plot is shown in Figure 4.5 a.

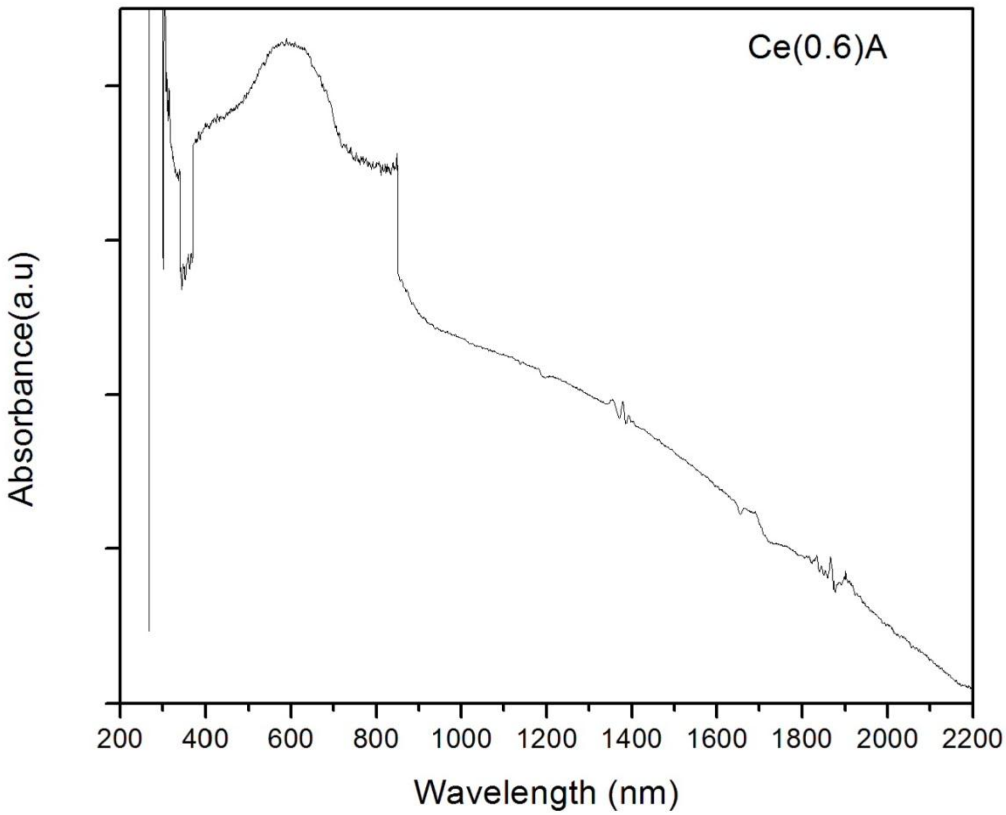

Figure 4.5 a Absorbance spectrum of $Sn_{1.4}Ce_{0.6}Sb_3$ sample

The tauc plot is analyzed for band gap. The discontinuity indicating the forbidden energy gap is seen and the band gap is calculated as 2.6eV. The region below is expanded for further analysis and is given in Figure 4.5 b.

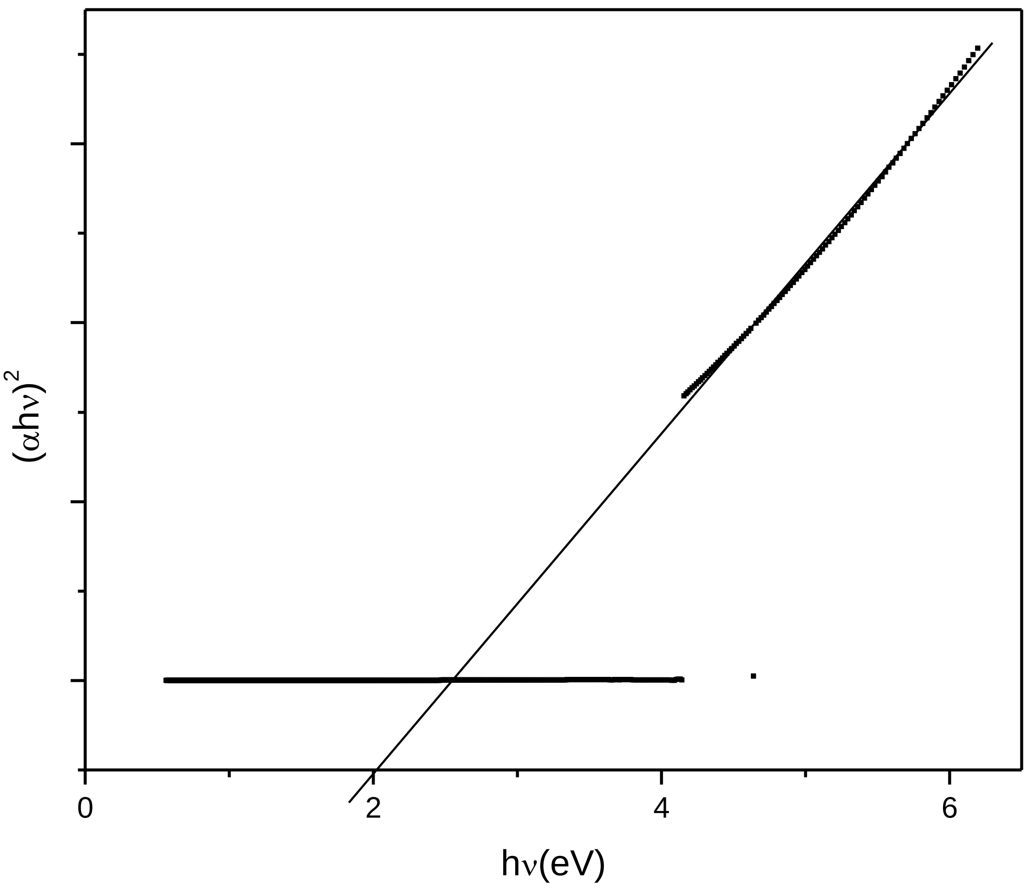

Figure 4.5 b. Tauc plot of $Sn_{1.4}Ce_{0.6}Sb_3$ showing the discontinuity in the energy levels

The energy gap of 2.01eV is observed for the $Sn_{1.4}Ce_{0.6}Sb_3$. Further analysis in lower energy side shows interesting effects due to the substitution of Cerium in the lattice which was not observed in the Sn_2Sb_3 sample.

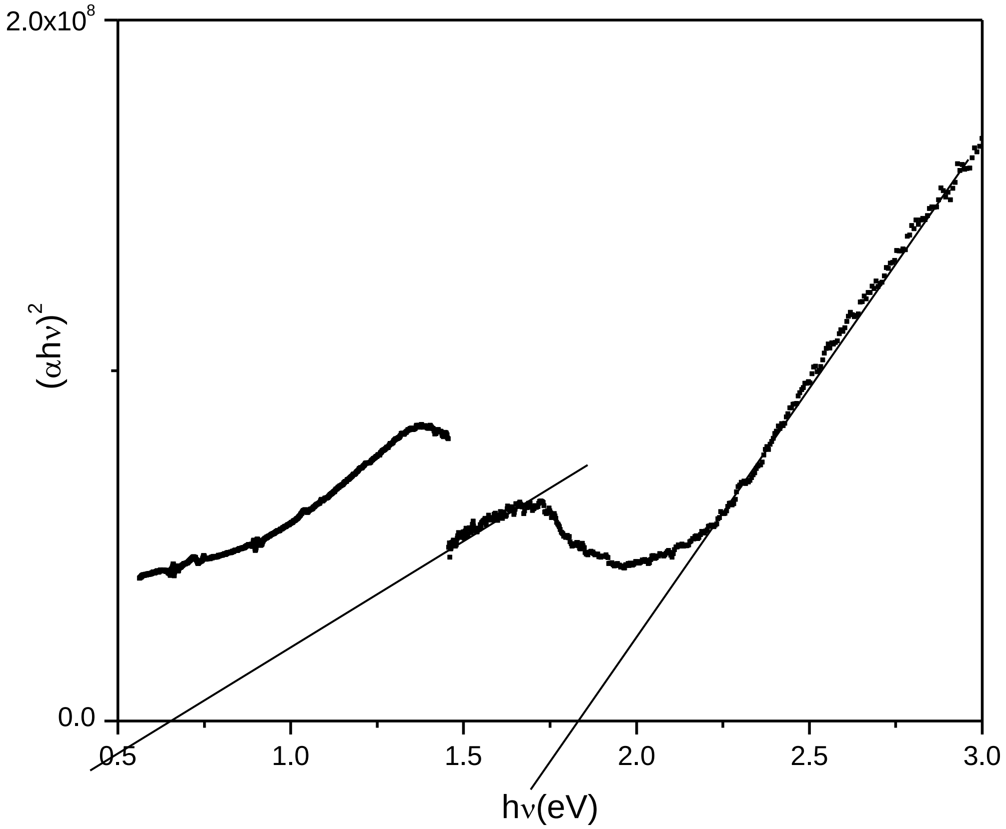

Figure 4.5c The discontinuity at deep level of energy observed in the $Sn_{1.4}Ce_{0.6}Sb_3$ sample

This shows another discontinuity with a band gap of 1.82eV originally due to the host of Sn_2Sb_3 that has been reduced due to the occupation of Cerium which reduced the forbidden gap to 0.65eV. A typical strain is also observed due to the mismatch between the Sn_2Sb_3 lattice and Cerium atoms. For reference, the energy band diagram of E vs k for both free electron and in a crystal lattice is shown here in Figure 4.6 (a,b). Consolidated band structure is shown in Figure 4.6c. Hence it is understood that there is a ground level S_0 and a band S_1 and S_2 are present. The effect of generated energy levels due to doping is seen between S0 and S1 bands very clearly. Thus the electronic band structure of the $Sn_{1.4}Ce_{0.6}Sb_3$ is clearly studied. Further analysis is made for the emission studies using photoluminescence studies.

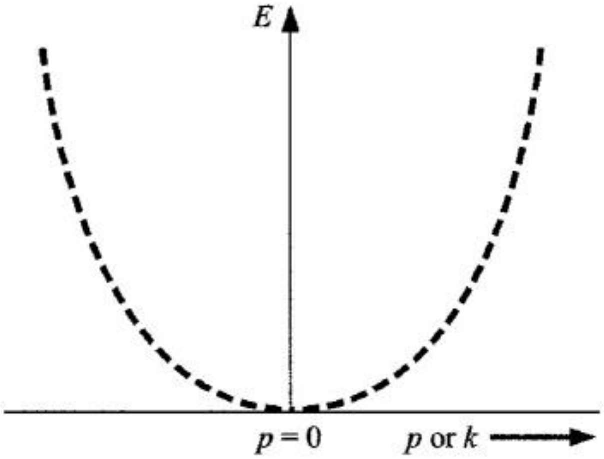

Figure 4.6 a E Vs k diagram for free particle with continuous energy levels

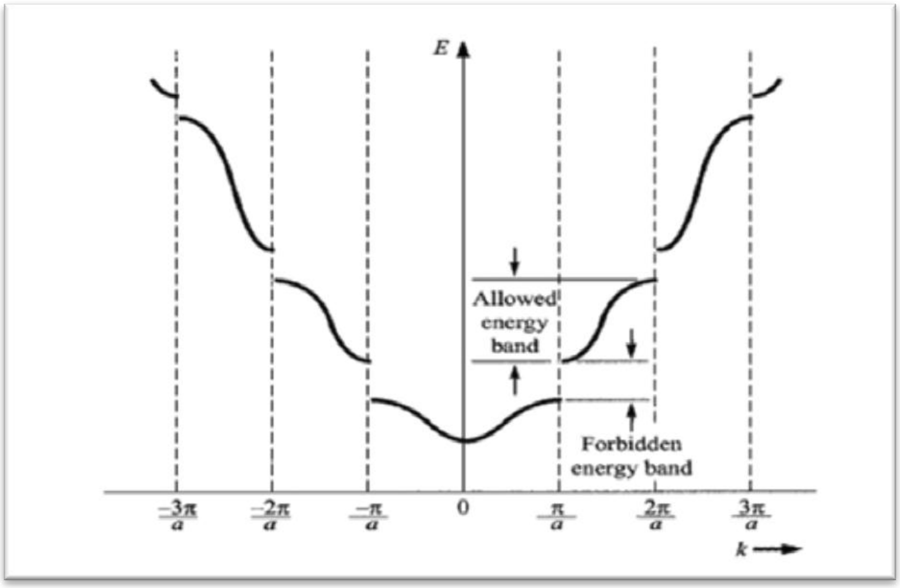

Figure 4.6b E Vs k diagram for crystal lattice with discontinuous energy levels

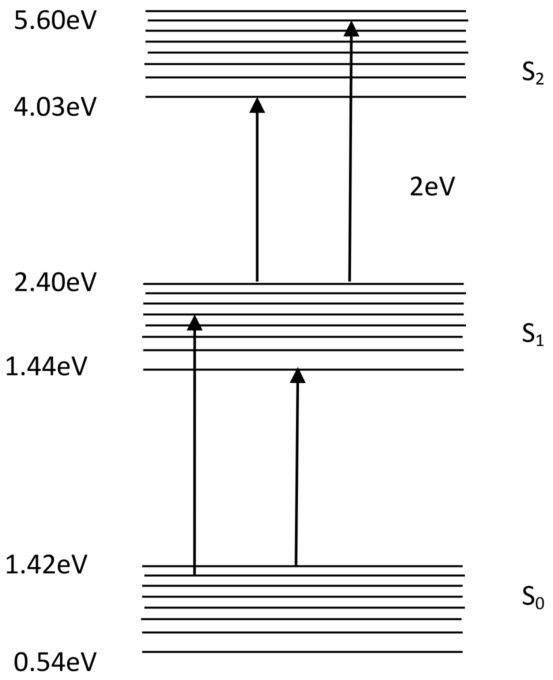

‘

Figure 4.6c Energy band structure as inferred from the tauc plot

4.4 Photoluminescence (PL) studies:

PL is studied for all the compositions but the transition for 0.6 composition has shown a difference in the tauc plot and hence the composition 0.6 alone is discussed here. The PL excitation of Sn_2Sb_3 sample at 340nm excitation is shown for reference in Figure 4.7a. The cerium substitution has made a broad emission from 400 nm to 550 nm when compared to the undoped. Thus a variation in emission profile that is favorable for any application in lighting is observed in this sample.

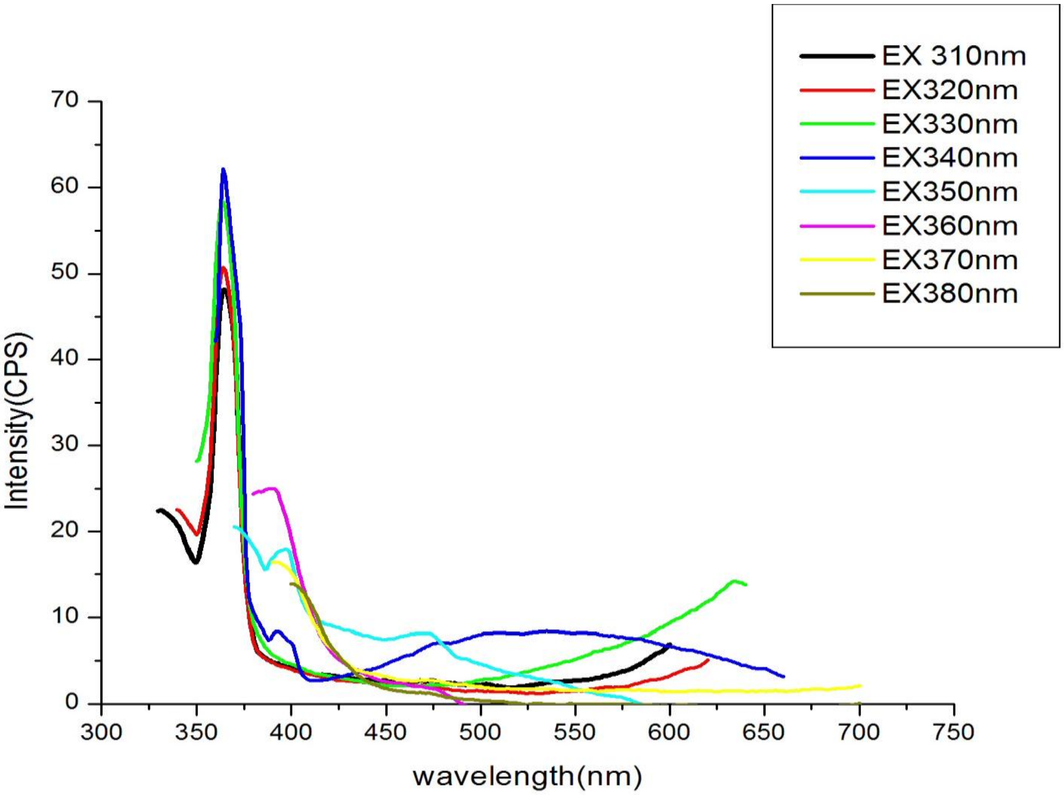

Figure 4.7.a PL emission of $Sn_{1.4}Ce_{0.6}Sb_3$ at different excitation wavelengths

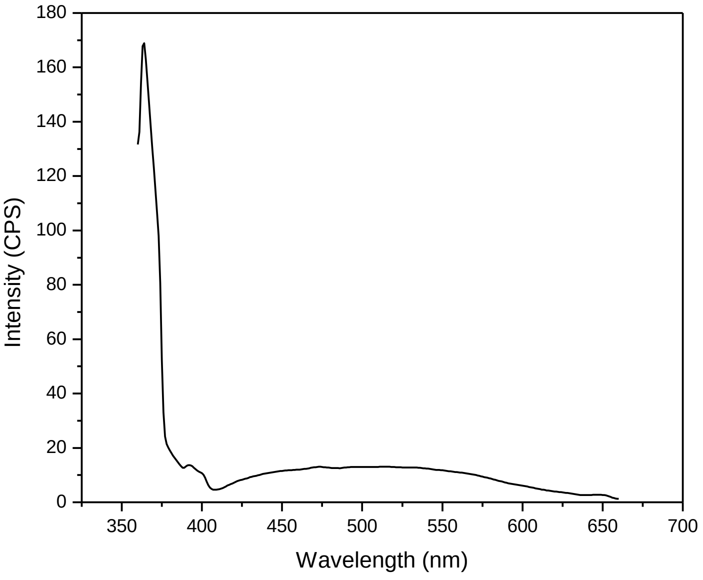

Figure 4.7.b PL emission of Sn_2Sb_3 at excitation at 340 nm

4.5 REFERENCES:

1. P. Nithyadharseni, B. Nalini, P. Saravanan, Applied Surface Science 311 (2014) 503–507
2. Laszlo Korosi, Szilvia Papp, Imre Dekany, Thin Solid Films 519 (2011) 3113–3118
3. YANG Fen, ZHANG Xue-jun, WU Xu, TIAN Fang, GAN Fu-xing, Trans. Nonferrous Met. Soc. China 17(2007)
4. Sutichai Chaisitsak, Sensors (2011), 11

SUMMARY AND CONCLUSION

CHAPTER V

SUMMARY AND CONCLUSION

5.1 Conclusion:

Sn_2Sb_3 and $Sn_{1.4}Ce_{0.6}Sb_3$ substituted samples are prepared by coprecipitation method, the phase is confirmed using X ray diffraction technique as rhombohedral. Irregularity in hexagonal structure is seen by the plane (004). The system is confirmed to be devoid of oxide through FTIR technique. The Absorbance and transmittance of the samples show that the energy bands of S0 S1 and S2 are found and their respective band gaps 2.0eV and 0.65eV persist. The band gap between S0 and S1 is altered from 1.85eV due to the additional allowed energy levels due to the doping to 0.65eV. The PL studies also show a favorable result of emission in visible region making this material a prospective one for lighting applications.